Overheating control in additive manufacturing using a 3D topology optimization method and experimental validation

Additive Manufacturing 61 (2023) 103339

Contents lists available at ScienceDirect

Additive Manufacturing

journal homepage: www.elsevier.com/locate/addma

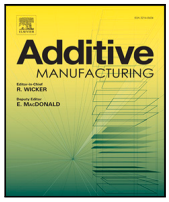

Research paper

Overheating control in additive manufacturing using a 3D topology optimization method and experimental validation

R. Ranjan [a,*], Z. Chen [b], C. Ayas [a], M. Langelaar [a], F. Van Keulen [a]

[a] Delft University of Technology, Mekelweg 2, 2628 CD Delft, The Netherlands
[b] Chalmers University of Technology, Chalmersplatsen 4, 412 96 Göteborg, Sweden

ARTICLE INFO

Keywords:
Additive Manufacturing
Topology optimization
Overheating avoidance
Optical tomography
Hotspot reduction
Thermal modelling of L-PBF

ABSTRACT

Overheating is a major issue especially in metal Additive Manufacturing (AM) processes, leading to poor surface quality, lack of dimensional precision, inferior performance and/or build failures. A 3D density-based topology optimization (TO) method is presented which addresses the issue of local overheating during metal AM. This is achieved by integrating a simplified AM thermal model and a thermal constraint within the optimization loop. The simplified model, recently presented in literature, offers significant computational gains while preserving the ability of overheating detection. The novel thermal constraint ensures that the overheating risk of optimized designs is reduced. This is fundamentally different from commonly used geometry-based TO methods which impose a geometric constraint on overhangs. Instead, the proposed approach takes the process physics into account. The proposed method is validated via an experimental comparative study. Optical tomography (OT) is used for in-situ monitoring of process conditions during fabrication and obtained data is used for evaluation of overheating tendencies. The novel TO method is compared with two other methods: standard TO and TO with geometric overhang control. The experimental data reveals that the novel physics-based TO design experienced less overheating during the build as compared to the two classical designs. A study further investigated the correlation between overheating observed by high OT values and the defect of porosity. It shows that overheated regions indeed show higher defect of porosity. This suggests that geometry-based guidelines, although enhance printability, may not be sufficient for eliminating overheating issues and related defects. Instead, the proposed physics-based method is able to deliver efficient designs with reduced risk of overheating.

1. Introduction

The unprecedented design freedom offered by additive manufacturing (AM) is ideal for fabricating performance optimized metal parts that are typically highly complex in geometry. Therefore AM has found extensive application in various industrial domains such as automotive, aerospace, sports and biomedical [1]. Although beneficial, the increased design freedom also makes the design process challenging and requires re-consideration of traditional design practices. Moreover, AM parts are typically utilized in hi-tech industry where the design process is inherently complex. This aspect along with the desire to capitalize on the increased design freedom, makes it advantageous to use advanced computational design tools. Topology Optimization (TO) is one such computational design method which aims to find the optimal material layout for a given design objective [2]. It is especially efficient for designing AM parts as it can address both functionality and manufacturability in a mathematically rigorous setting. Due to this, the potential of combining TO and AM has been recognized by both academia and industry [3].

Although AM processes offer several key advantages over conventional methods, there are certain manufacturing constraints which, if not addressed during the design stage, could lead to inferior part quality or build failure [1]. One such constraint which has been extensively studied within TO frameworks is that of overhang avoidance. Design rules associated with overhang angles, defined as the angle between part surface and horizontal base plate, have been empirically developed [4]. It is recommended that the overhang angle should be higher than a certain critical value θ^{cr}, typically ranging between 40°–50° [5,6]. Features with acute overhangs are difficult to fabricate for both polymer and metal based AM processes, although the fundamental causes behind the difficulty of their fabrication vary. For extrusion based polymer AM, such as fused deposition modelling (FDM), the overhanging regions lack sufficient supports against gravity. On the

* Corresponding author.
E-mail address: r.ranjan@tudelft.nl (R. Ranjan).

https://doi.org/10.1016/j.addma.2022.103339
Received 11 June 2022; Received in revised form 23 November 2022; Accepted 29 November 2022
Available online 9 December 2022

other hand, in powder based metal AM processes, such as Laser Powder Bed Fusion (L-PBF), loose powder beneath an overhanging feature provides structural support but the low and non-uniform thermal conductivity of powder does not allow for proper heat evacuation [4]. This leads to severe local overheating which manifests itself in form of defects, *e.g.* dross [7], inferior mechanical properties [8], increased surface roughness [7] and/or build failure [9]. In this paper, we aim to investigate the issue of local overheating and hence, in the remainder, we focus on the L-PBF process where this is a critical issue. Note that in certain cases, for example Mohr et al. [8], the heat accumulation over the layers may have a positive effect such as in-situ heat treatment improving the properties. However, generally local overheating is associated with increased risk of defects and therefore our focus is to reduce the amount of overheating. In this context, recent advancements in L-PBF machines allows for in-situ control of laser power reducing the risk of overheating. However, this feature is currently under development and not a default option. Hence, part geometries with low overheating risks are still highly desirable.

In the context of TO, a significant number of studies have been presented in literature which aim to integrate overhang avoidance within TO algorithms, see, for example, Gaynor and Guest [10], Wang and Qian [11], Langelaar [12], Langelaar [13] and van de Ven et al. [14]. These methods prohibit or penalize overhanging features less than the critical overhang angle during the optimization process, improving the manufacturability of the optimized designs. For a detailed review of these and related methods, see Liu et al. [3]. These formulations, referred to as geometry-based TO, use overhang detection for avoiding acute overhangs under the assumption that geometric overhang control ensures printability. However, recent experimental and numerical findings indicate that overheating can occur even after avoiding acute overhangs. For example, Adam and Zimmer [15] fabricated a funnel shaped specimen in which overheating was observed in the form of discolouration. Another specimen by Patel et al. [16] showed overheating induced dross. It is noteworthy that specimens in both cases were free from acute overhangs. A recent numerical study by Ranjan et al. [17] demonstrated that overheating behaviour associated with the same overhang angle can vary significantly, depending on local thermal conditions. These findings suggest that the relationship between overhang and overheating is not straightforward. Hence, a TO method which focuses directly on the issue of overheating will offer significant advantages over geometry-based TO methods.

A detailed thermal L-PBF process model is required to capture the overheating issues in a part during the additive fabrication process. It is well known that L-PBF process models are computationally expensive (see, for example, Denlinger et al. [18] and Keller and Ploshikhin [19]). Moreover, integration of such elaborate models within TO is especially cumbersome, as the simulation should be repeated for each design iteration, and design sensitivities must be calculated in addition. Therefore, developing simplified AM models which can capture essential aspects of the thermal evolution is of paramount importance, making it possible to integrate such models with TO. This leads to the so called physics-based TO methods which incorporate to some extent the physics of the AM process. Research presented by Amir and Mass [20] and Allaire et al. [21] are examples of such approaches, where self-weight of the manufactured part is considered in a layer-by-layer manner, mimicking the real process. In the context of overheating control, Zhou et al. [22] integrated simplified thermal AM simulation with density-based TO for finding optimal supports, while keeping the part design fixed. However, even with several simplifications, the computational cost remained significantly high, even for a 2D implementation. More recently, Boissier et al. [23] coupled a simplified thermal model with 2D level-set TO where scanning path optimization is performed. Although it provides insights about influence of scanning paths on temperatures, it is expected that computational cost remains high. In this regard, the simplified model presented by Ranjan et al. [17] which used a localized *slab based* steady-state thermal analysis is suitable for detecting overheating zones (hotspots) at relatively low computational cost. Therefore, it has been integrated with density based TO and the concept has been investigated in Ranjan et al. [24], where it is referred to as hotspot TO. The aim of the present paper is to experimentally compare the overheating tendencies associated with the hotspot TO design against those observed for the designs obtained using other TO strategies. In this context, the 'AM-filter' method presented by Langelaar [12] and Langelaar [13], which is an example of geometry-based TO, and standard TO without any AM constraint are considered for experimental comparison. For the experimental investigation, optical tomography is used to monitor manufacturing conditions during fabrication.

Optical tomography (OT) is an in-situ technique to monitor the L-PBF process and detect overheating resulting from the heat accumulation. It is a camera-based measurement technique for the observation of the thermal radiation over the process plane while the laser beam scans the powder bed surface [25]. Deviations in the measured signals can be derived from the OT images as implications of process anomalies where internal defects can be formed in the manufactured products [26,27]. The detection of hotspots is of particular interest in this work for the comparison of different TO strategies for avoiding overheating. Additionally, to the best of our knowledge, this is the first research study where a physics-based TO method is experimentally validated using the OT technique.

The remainder of the article is organized as follows. The physics-based hotspot detection method and formulation of overheating constraint are presented in Section 2. The simplified AM model which was previously presented in Ranjan et al. [17] and Ranjan et al. [24] is briefly summarized for completeness. Different TO strategies and the test problem considered for comparing optimized designs are presented in Section 3. The details associated with the experimental procedure are given in Section 4, while the comparative results are presented in Section 5. Finally, discussion and conclusions are presented in Sections 6 and 7, respectively.

2. Hotspot detection

Here, we first summarize our simplified L-PBF process model for detecting heat accumulation. The model is taken from our previous study [17] where several simplifications associated with thermal modelling of the L-PBF process were investigated in context of detecting overheating. It was established that hotspot detection is possible by computationally inexpensive steady-state local thermal analyses near the heat source [17]. Although the thermal fields in an actual L-PBF process are more accurately predicted with a transient thermal model, their integration with design optimization methods is highly cumbersome as shown by Van Keulen et al. [28], making it computationally intractable for real-size 3D parts. Consequently, the steady-state model which correctly identifies overheating zones is a perfect candidate for integration with topology optimization.

The part shown in Fig. 1(a) is used to demonstrate the simplified L-PBF thermal model. This design results from an AM-filter geometry-based TO method [13]. We purposefully choose this design for explaining the simplified model as it has several features with overhang angles close to the threshold value of $\theta^{\mathrm{cr}} = 45°$. Therefore, it enables a close examination whether the same overhang angle leads to similar overheating behaviour. Fig. 1(c)–(f) show subsequent stages of L-PBF fabrication where the part is divided into a set of so-called *slabs* represented by yellow coloured bounding boxes with *slab thickness* s. These slabs are defined such that subsequent slabs largely overlap, compare for example, Fig. 1(c) and (d). The section of the part inside a slab is subjected to a steady-state thermal analysis where the top surface is subjected to a heat flux $\mathbf{q}_0$ (indicated by red arrows) and the bottom of the slab acts as a heat sink (indicated by black boundary). These boundary conditions are inspired by the L-PBF process where heat is deposited from the top layer using a laser, while previously deposited

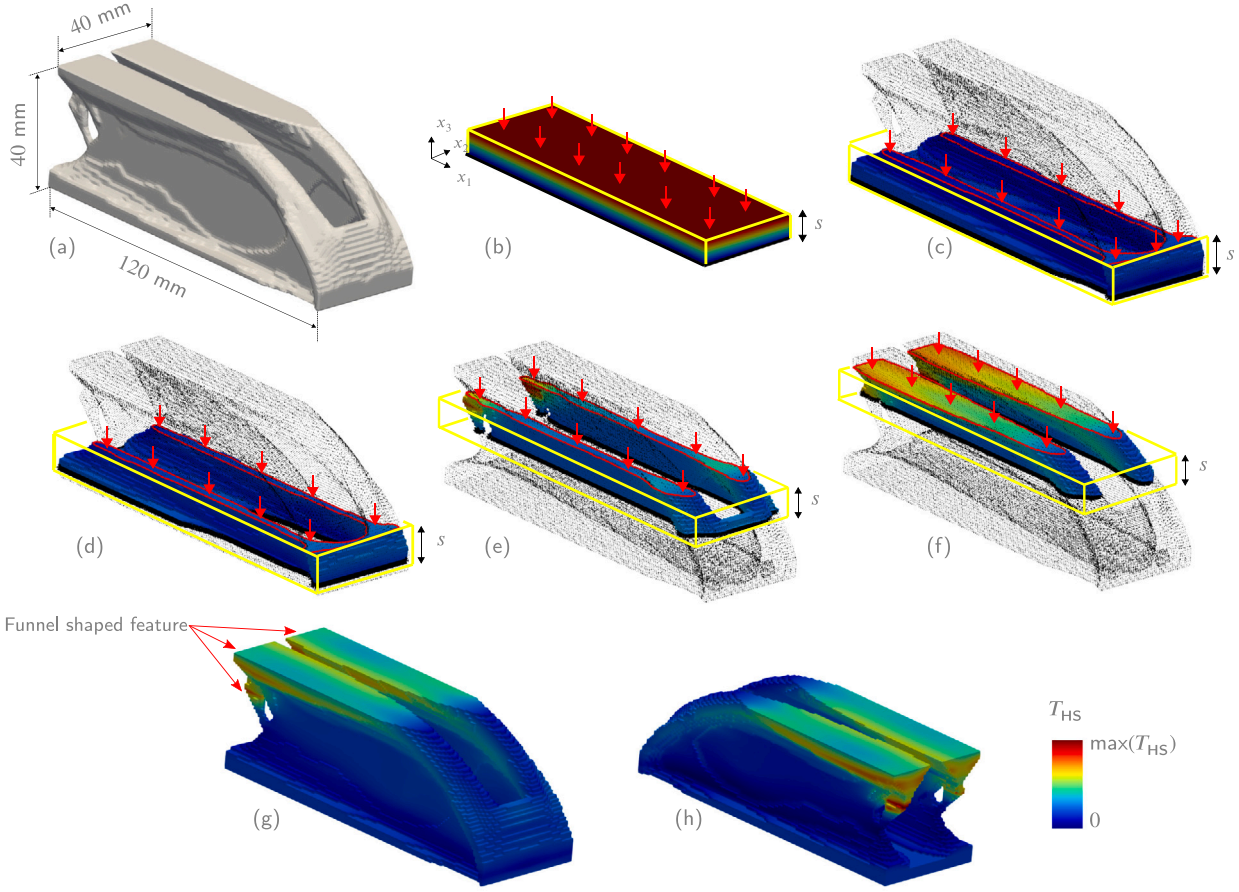

Fig. 1. Simplified AM model for detecting heat accumulation using slabs [17]. (a) Part considered for explaining the method. (b) A solid slab used for obtaining normalized temperatures is shown with corresponding temperature gradients. (c)–(f) Subsections of the geometry with contour levels of temperature attained with a steady-state thermal analysis. For each slab heat flux is applied at its top (indicated by arrows) while its bottom acts as a heat sink (indicated by black boundaries). Part-powder interfaces are assumed to be insulated. The maximum temperature for each material point is recorded and the resulting maximum temperature field is referred to as hotspot field T_{HS} which is shown from front (g) and back (h). The funnel shaped features which lead to high normalized temperatures are indicated with red arrows in (g).

layers and baseplate act as a heat sink. A list of simplifications which are assumed in addition to the use of localized steady-state analysis is given below:

- Laser scanning path is not considered for computational efficiency, following layer-by-layer L-PBF modelling approaches [17,29].
- Thermal properties are assumed to be constant and hence independent of temperatures.
- Part-powder interface is assumed to be insulated as effective conductivity for powder layer is reported to be around only 1% of bulk conductivity [30,31].
- Phase transformations are not considered.
- Convective and radiative heat transfer from the top surface are not considered.

In order to verify the usefulness of the simplified L-PBF model, a brief comparison is presented between thermal predictions of the simplified model and a higher-fidelity transient L-PBF simulation later in Section 3.2.5. It shows that a model with these simplifications can still correctly predict which design features are at the risk of overheating. Additionally, a deeper and quantitative study of various modelling simplifications is presented in Ranjan et al. [17] where detailed rationalizations are provided about each of the above listed simplification in the context of overheating detection.

Under these simplifications, the temperatures are calculated using the 3D steady-state heat equation [32]. The partial differential equation (PDE) is solved numerically using finite element analysis (FEA) and resulting temperature fields are shown in Fig. 1(c)–(f). The details on the finite element mesh for solving the thermal problems are given in the next section. Due to the overlapping definition of slabs, every material point is analysed multiple times within different slabs, leading to multiple temperature values for each point. These temperatures depend on the local effective conductivity of the neighbourhood and the maximum value attained for each point is attributed to the overheating risk associated with that point. Due to the considered boundary conditions, the maximum temperature for the steady-state thermal field always occurs at the topmost layer of each slab. Therefore, temperatures found at the topmost layer from each slab are assembled into a *hotspot field* for the given geometry. The hotspot field for the considered geometry is shown in Fig. 1(g) and (h) as seen from the front and back, respectively. Note that all thermal fields are shown with a common scale ranging from sink temperature T_0 to the maximum value observed across all slabs.

It is noteworthy that the funnel like features, marked with arrows in Fig. 1(g), lead to high temperatures even though they comply with the overhang design rule, yet their thermal response is not uniform. A more quantitative analysis of the found hotspot field is given later in Section 3.2.4, where hotspot fields for all topology optimized designs are compared.

As the above summarized L-PBF model is a simplified steady-state representation of the thermal interactions during the process, the resulting predictions do not quantitatively describe the actual temperature field during the process. Instead, they simply give a qualitative indication about the overheating risk associated with different design features [17]. In order to formulate an overheating constraint in TO,

a threshold value needs to be specified. Therefore, a normalization step is introduced where temperatures from each slab are normalized against those found using a solid slab containing no void with the same thermal properties and subjected to the same thermal boundary conditions. An example of such temperature field is shown in Fig. 1(b). A solid slab with no void represents the ideal situation of unobstructed heat flow. Thus, the hotspot temperatures normalized against such a solid slab quantify the heat accumulation tendencies. This implies that the normalized temperature is dimensionless and values greater than 1 indicate overheating with increasing severity. Moreover, the normalized temperature values are independent of the input heat flux $\mathbf{q}_0$, the sink temperature and the thermal conductivity as the solid slab used for normalization has identical thermal properties and is subjected to the same thermal boundary conditions.

The slab thickness parameter represents the *thermal interaction length* κ *i.e.*, the distance up to which features influence the heat flow at the newly deposited layer. For L-PBF, thermal interaction length is significantly higher than the layer thickness [33]. From this observation follows that subsequent slabs overlap each other considerably. The slab thickness value depends on material and process parameters. For example, a material with lower thermal diffusivity is better modelled with thin slabs as compared to one with higher thermal diffusivity. Alternatively, a slow moving laser would allow for more thermal interaction time and hence, larger interaction distances. In Ranjan et al. [17], using an analytical solution to the heat equation, it was shown that thermal interaction length can be estimated as $\kappa = \sqrt{\alpha t_h}$, where α is the thermal diffusivity and t_h is the heating time for a given layer. The heating time for a layer further depends on a number of factors, *e.g.* , layer area, laser speed, number of lasers etc. More recently in Ranjan et al. [24], this concept was used for determining slab thickness in context of TO and a detailed analysis was provided on the influence of this parameter on TO results. In this paper, we used the same concept to determine slab thickness and the methodology is summarized below for the sake of completeness.

First, based on the building direction, maximum layer area A is determined for the design domain which is then used for calculating heating time as $t_h = A/h\upsilon$, where h is hatch spacing and υ is scan velocity. The parameters used in this study are reported later in Section 4. Next, based on the concept of thermal characteristic length, slab thickness is calculated as $\kappa = \sqrt{\alpha t_h}$. The thermal diffusivity α is calculated using thermal properties reported at melting point temperatures [34]. This is motivated by the findings of Yang et al. [35] which showed that using an α value close to the melting point gives the best thermal predictions when using temperature independent thermal properties.

3. Topology optimization

In this section, first the test problem considered for comparing different TO strategies is introduced in Section 3.1. The mathematical formulation for TO is also presented here and different TO algorithms considered in this paper are described. The physics-based TO is explained in more detail than the other two more established approaches. Next, the TO results for the test problem are presented in Section 3.2.

3.1. Test problem and TO approaches

In this paper, we consider topology optimized designs using three different TO approaches, *i.e.*, standard TO, hotspot TO (physics-based TO) and AM-filter TO (geometry-based TO). As the main focus here is to analyse the overheating tendencies of different designs during L-PBF fabrication, the discussion is restricted to the commonly used linear elastic compliance minimization problem with a volume constraint which is a structural optimization problem.

The standard density based TO approach using SIMP interpolation [2] scheme is applied as:

$$\min_{\boldsymbol{\rho}} : \; C(\boldsymbol{\rho}) = \mathbf{u}^T \mathbf{K}\mathbf{u}, \tag{1a}$$

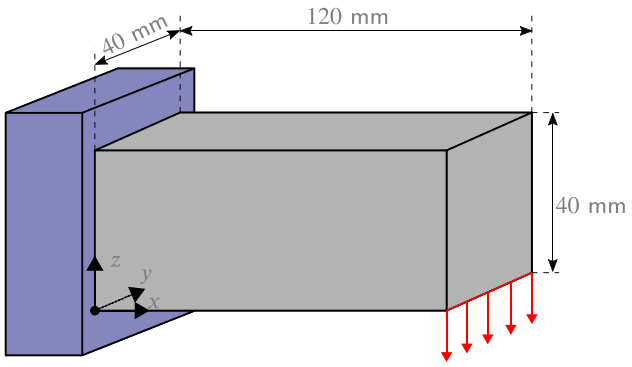

Fig. 2. The test problem used for creating optimized designs using different TO approaches.

subject to (1b)

$$\frac{V(\boldsymbol{\rho})}{V_o} - f_o \leq 0, \tag{1c}$$

$$\mathbf{K}\mathbf{u} = \mathbf{f}, \tag{1d}$$

$$\mathbf{0} \leq \boldsymbol{\rho} \leq \mathbf{1}. \tag{1e}$$

Here, C is the compliance, $\mathbf{u}$ and $\mathbf{f}$ are the arrays containing the nodal displacements and forces, respectively, $\mathbf{K}$ is the global stiffness matrix, $\boldsymbol{\rho}$ is the array of design variables assigned to FE elements, $V(\boldsymbol{\rho})$ and V_0 are the total material volume and design domain volume, respectively, and f_o is the maximum volume fraction allowed in the design domain. The optimization problem is initiated with uniform density of $\boldsymbol{\rho} = f_o$. The density filtering scheme presented by Bruns and Tortorelli [36] is used with filter radius $R = 2$ mm in order to control minimum feature size and avoid checkerboarding. The Matlab 3D TO implementation presented by Liu and Tovar [37] is used for solving this optimization problem while the method of moving asymptotes (MMA) is used as the optimizer [38].

A cantilever loading case is considered with a design domain with dimensions 120 × 40 × 40 mm as shown in Fig. 2. Here, a 40 N load is uniformly distributed over the lower front edge while the back face ($x = 0$) remains fixed. The domain is discretized using isoparametric cubic 8-node finite elements with tri-linear shape functions with 120, 40 and 40 elements in x, y and z directions, respectively. All common TO parameters are listed in Table 1. Note that Fig. 2 only presents the design domain and the resulting optimized cantilever beams are presented later in Section 3.2.

In case of the physics-based TO, an additional constraint is formulated which is referred to as the hotspot constraint. It is added in the standard optimization problem given in Eqs. (1) and its formulation is explained below. During physics-based TO, each intermediate design is subjected to the hotspot analysis described in Section 2. The structured mesh used for solving the structural problem is also used for the thermal analysis. All normalized temperatures from the hotspot analysis are stored in an array denoted as $\hat{\mathbf{T}}$. In order to avoid local overheating, it is required that the normalized temperatures should not exceed a critical value $\hat{T}^{\text{cr}}$, *i.e.* $\max(\hat{\mathbf{T}}) \leq \hat{T}^{\text{cr}}$. Note that the max operator is non-differentiable whereas a smooth operator is required for calculating the sensitivities needed in gradient based TO. Therefore, a P-mean aggregation is performed over the array $\hat{\mathbf{T}}$ to define the hotspot constraint:

$$g = \left[\frac{1}{n\hat{T}^{\text{cr}}} \sum_{i=1}^{n} \hat{T}_i^P\right]^{\frac{1}{P}} - 1 \leq 0. \tag{2}$$

Here, $\hat{T}_i$ is the ith member of array $\hat{\mathbf{T}}$, P is the exponent used for defining the P-mean and n is the total number of nodes considered. Recall that the maximum temperature always occurs at the topmost

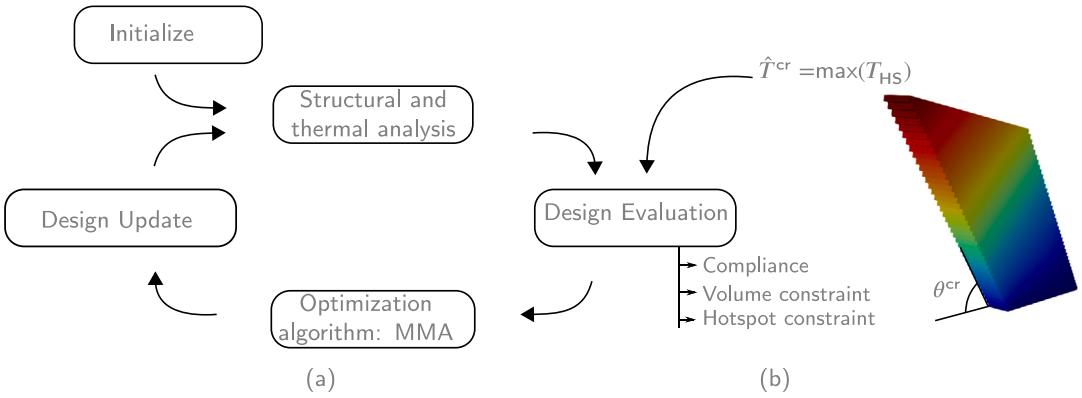

Fig. 3. Schematic illustrating the hotspot TO framework and critical temperature calibration. (a) The steps associated with the TO algorithm with additional hotspot analysis and constraint. (b) 2.5D wedge geometries are used to determine associated $\hat{T}^{cr}$ with a particular θ^{cr}.

Table 1
Topology optimization parameters.

Poisson's ratio	0.3
SIMP penalization	3.0
Volume fraction f_o	0.3
P-mean exponent P	15
Slab thickness s (mm)	12
No. of iterations	200

layer of each slab, hence, only top nodes from each slab are considered in the aggregation. The sensitivity derivation for the hotspot constraint is presented in Appendix A.

For determining the critical normalized temperatures $\hat{T}^{cr}$, a calibration step was proposed in Ranjan et al. [24] which is used here. Typically, a critical overhang angle for a given L-PBF system is determined by experimental studies [5,6]. Here, an L-PBF system refers to a combination of material and process parameters and such empirical studies basically signify that the thermal conditions while manufacturing overhangs with an overhang angle $\theta < \theta^{cr}$ can lead to fabrication difficulties. In order to determine the critical overhang angle for a system, it is a common practice to use a 2.5D wedge shape where a 2D wedge with a certain overhang angle is simply extruded in the out-of-plane direction [5,6]. Following a similar approach for numerically determining $\hat{T}^{cr}$, the calibration step presented for 2D wedges in Ranjan et al. [24] can be directly applied to 3D. Wedge-shaped geometries, see Fig. 3(a), with varying wedge inclinations were subjected to hotspot analysis and corresponding normalized hotspot temperatures were used as $\hat{T}^{cr}$. It is worth emphasizing that this does not correspond to geometrically prohibiting overhanging features less than a specific overhang angle, as it is done in the geometry-based approaches [12]. Instead, the *thermal behaviour* associated with an overhanging feature is used to set the hotspot temperature threshold. A schematic is shown in Fig. 3 where the calibration process is pictorially presented in (a) while (b) shows how the hotspot constraint is integrated with the TO process. Using this calibration step, $\hat{T}^{cr}$ for three different values of θ^{cr}, *i.e.*, 40°, 45° and 50°, are found to be 2.5, 2.1 and 1.8, respectively. These values are later used in Section 3.2.3.

Next, it was highlighted in Ranjan et al. [24] that when a hotspot constraint is implemented in combination with standard TO, this may result in designs with significant amount of intermediate densities. A design with high fractions of intermediate densities becomes problematic for fabrication [2]. In order to solve this issue, the robust formulation presented by Wang et al. [39] and Sigmund [40] was used with $R = 5$ mm. Slab thickness $s = 12$ mm is used for all the cases, calculated in accordance with the concept of thermal characteristic length using the constant thermal properties of Inconel 718 at melting point.

Lastly, the AM-filter TO presented by Langelaar [12] is considered as an example of geometry-based overhang control TO method. The method basically imposes a progressive layer-wise filtering scheme during TO iterations which results in fully self-supported optimized designs. In this regard, the basic TO problem remains the same as outlined by Eqs. (1) while one additional filtering step is added. For the details of the mathematical formulation of AM-filter, readers are referred to Langelaar [13] and Langelaar [12].

3.2. Optimized TO designs and hotspot fields

In this subsection, all the topology optimized designs which are subsequently fabricated and monitored using OT are presented. The density fields obtained from TO are post-processed for visualization by extracting iso-surfaces with a threshold value of 0.5. As the standard TO result is used as a benchmark for comparing compliances of the optimized designs, it is presented first with compliance referred to as C_{ref}. A comparison of hotspot fields for all TO designs is presented in Section 3.2.4.

3.2.1. Standard TO

Fig. 4 shows the optimized beam while a section view with a sectioning plane at $y = 20$ mm is also given for clear visualization of inner features. The build direction (z) is marked and it is evident that there is a long overhanging feature near the top region of the design (marked in red). It is expected that fabrication of such a long overhang, without any supports, will be extremely problematic due to excessive heat accumulation.

3.2.2. Geometry-based TO for overhang avoidance

The test problem given in Section 3.1 was optimized in the original paper by Langelaar [12] and the resulting design is presented in Fig. 5. In order to clearly visualize the optimized design, a section view at $y = 20$ mm is also presented. The method uses a structured mesh with cubic elements leading to $\theta^{cr} = 45°$. It is evident that the AM-filter design is free from the extensive overhangs present in the standard TO design and it is expected that it can be realized without the need of any additional supports. Typically, inclusion of additional process constraints into the TO process leads to reduced performance, *i.e.* higher compliance (for this case). This is seen as a compromise between manufacturability and design freedom. Between the standard and AM-filter TO designs, remarkably the latter slightly outperforms the former. This has also been observed previously [12] and is caused by potentially finding a better local optimum in combination with a reduction of intermediate density elements at the structural boundaries, due to the applied filter. Lastly, as highlighted in Section 2, this design contains several funnel shaped features, where the overhang angle is close to the limiting value, *i.e.* $\theta^{cr} = 45°$.

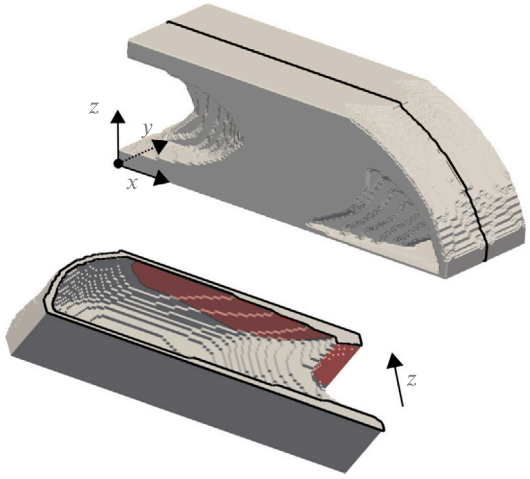

Fig. 4. The optimized beam using standard TO outlined by Eqs. (1) with $C = C_{\text{ref}}$. The highlighted red region shows significantly long overhangs that are present in this design.

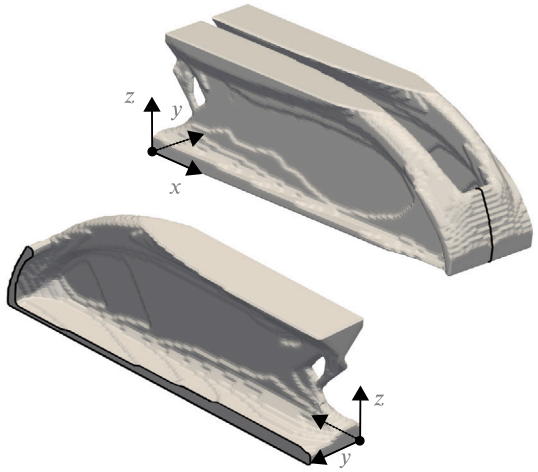

Fig. 5. The optimized design found using AM-filter [12] with $C = 0.92C_{\text{ref}}$. It is evident the method ensures manufacturability by avoiding long overhangs, present in the standard TO design.

3.2.3. Hotspot TO

For the TO with hotspot constraint, three different values of $\hat{T}^{\text{cr}}$ are used based on three values of θ^{cr}, *i.e.*, 40°, 45° and 50°. As presented in Section 3.1, $\hat{T}^{\text{cr}}$ for 40°, 45° and 50° are found to be 2.5, 2.1 and 1.8, respectively. This leads to three optimized designs shown in Fig. 6 with $\hat{T}^{\text{cr}}$ used for 40°, 45° and 50°. In the remainder, these designs are referred to as HS XX, where XX denotes the overhang angle used for setting up $\hat{T}^{\text{cr}}$. HS 40, HS 45 and HS 50 are shown in Fig. 6(a)–(c) while their section views are shown in Fig. 6(d)–(f), respectively. The HS 45 design is later compared with the AM-filter design as both are based on $\theta^{\text{cr}} = 45°$ as threshold. The final compliances for HS 40, HS 45 and HS 50 are found to be $C = 2.3C_{\text{ref}}$, $C = 2.6C_{\text{ref}}$ and $C = 3.2C_{\text{ref}}$, respectively. The compliances show an increasing trend with higher θ^{cr} or lower $\hat{T}^{\text{cr}}$ implying that a stricter constraint leads to reduced design freedom and hence, a performance penalty. This was also previously discussed in Ranjan et al. [24]. Next to the restriction imposed by the hotspot constraint itself, unlike the standard and AM-filter design, the hotspot TO process requires a robust formulation. This results in additional restrictions on minimum length scale and solution space [39]. The difference in mechanical performance is therefore expected. However the primary focus on this paper is on the differences in thermal behaviour during printing between designs produced by the three TO methods, as analysed below.

3.2.4. Comparison of hotspot fields

This section is divided into three sets of comparisons between hotspot fields of the presented TO designs. The first set compares standard TO, AM-filter and HS 45 designs, with their corresponding hotspot fields shown in Fig. 7(a)–(c). For sake of comparison, all normalized temperatures are scaled between 0 and the maximum value obtained across these designs which is found to be $\hat{T} = 11.6$ for standard TO. It is clearly seen that the long overhang towards the back of the standard TO design leads to extremely high normalized temperatures. Contrary to this, the other two designs remain significantly cooler, signifying that both geometry and physics-based TO methods enhance printability. However, since both AM-filter and HS 45 designs are at significantly lower normalized temperatures compared to the standard TO, it is difficult to compare between Fig. 7(b) and (c). Therefore, in Fig. 7(d)–(f), these two designs are shown again but with normalized temperatures scaled between 0 and 4.2, which is the maximum value obtained for AM-filter design. For the AM-filter design, the funnel like features which remain close to the threshold overhang angle value of 45° lead to high normalized temperature values in Fig. 7(d). Note that the critical temperature found for $\theta^{\text{cr}} = 45°$ using the calibration step is $\hat{T}^{\text{cr}} = 2.1$, which is used for defining hotspot constraint given by Eq. (2). However, normalized temperatures for the AM-filter design exceed this value, signifying that this design violates the hotspot constraint. The AM-filter design with regions which overshoot beyond the $\hat{T}^{\text{cr}} = 2.1$ are highlighted in Fig. 7(e). Compared to this, the HS 45 design, shown in Fig. 7(f), remains below the highest value prescribed by the hotspot constraint. Lastly, for presenting the thermal gradients within the hotspot TO designs and highlighting the influence of $\hat{T}^{\text{cr}}$, HS 40, HS 45 and HS 50 designs are shown in Fig. 7(g), (h) and (i), respectively. Here, normalized temperatures are scaled between 0 and the maximum value attained for each design. It is evident that short near-horizontal overhangs which do not violate the hotspot constraint are allowed to exists in these designs.

3.2.5. Evaluation using higher fidelity transient L-PBF model

In order to evaluate the thermal performance of different optimized designs and to verify the performance of the simplified L-PBF model, the three designs are subjected to a higher fidelity transient L-PBF simulation based on a layer-by-layer deposition strategy. Unlike the simplified approach, this model considers losses due to convection and radiation. Moreover, variation of thermal properties with respect to temperature is also considered. Details about the process parameters used for higher fidelity simulation can be found in Ranjan et al. [17]. The material properties for Inconel 718 are taken from Agazhanov et al. [34].

Following the same logic presented while discussing the simplified steady-state L-PBF model, the maximum temperature is picked for each spatial point across all time steps for preparing the hotspot field for each design. Fig. 8 shows the found hotspot fields for the standard TO, AM-filter and HS 45 designs. In order to compare, 8(a), (b) and (c) present the results with common temperature scale ranging between baseplate temperature and maximum attained for standard TO part. Regarding hotspot location and relative intensity, the higher fidelity simulation results are in agreement with those shown in Section 3.2.4 where the simplified model detected the worst hotspot in the standard TO design. Next, in order to highlight the gradient within the part, 8(e) and (f) show the temperature fields ranging between baseplate value and maximum obtained for AM-filter and HS 45, respectively. Again, it can be observed that funnel shapes for the AM-filter design are identified as hotspots with maximum temperature occurring at same locations as predicted by the simplified steady-state model (see Fig. 1(g)). However, a deeper comparison between 8(e) and Fig. 1(g) shows that overall spatial distribution of hotspot temperatures is different when

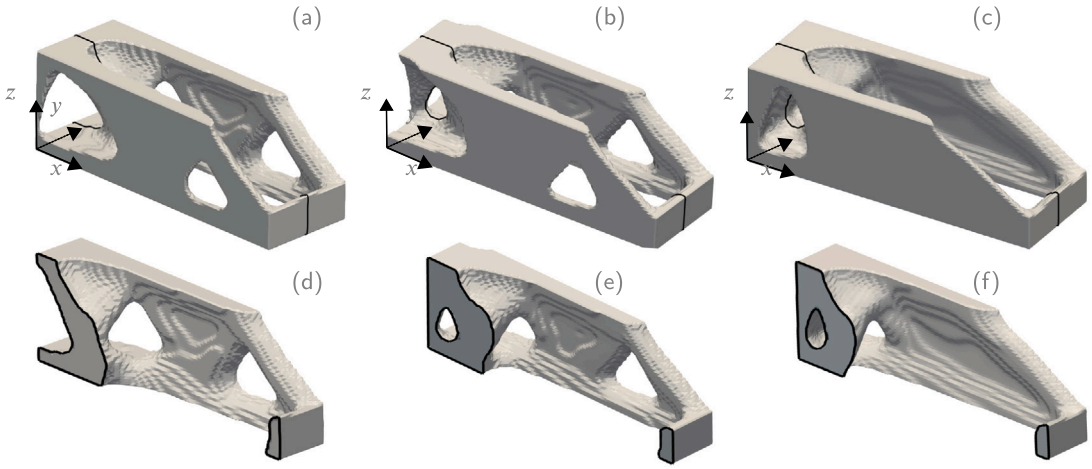

Fig. 6. The optimized beam using hotspot TO presented in Section 2. These designs use three different critical normalized temperatures and hence, are referred to as HS XX, where XX stands for the overhang angle used to set critical temperature. Using this nomenclature, designs shown in (a) HS 40 is found using $\hat{T}^{cr} = f(\theta^{cr} = 40°)$ resulting in $C = 2.3C_{ref}$ (b) HS 45 is found using $\hat{T}^{cr} = f(\theta^{cr} = 45°)$ resulting in $C = 2.6C_{ref}$ (c) HS 50 is found using $\hat{T}^{cr} = f(\theta^{cr} = 50°)$ resulting in $C = 3.2C_{ref}$. Section view with section at $y = 20$ mm are given in (d) (e) and (f) for HS 40, HS 45 and HS 50, respectively.

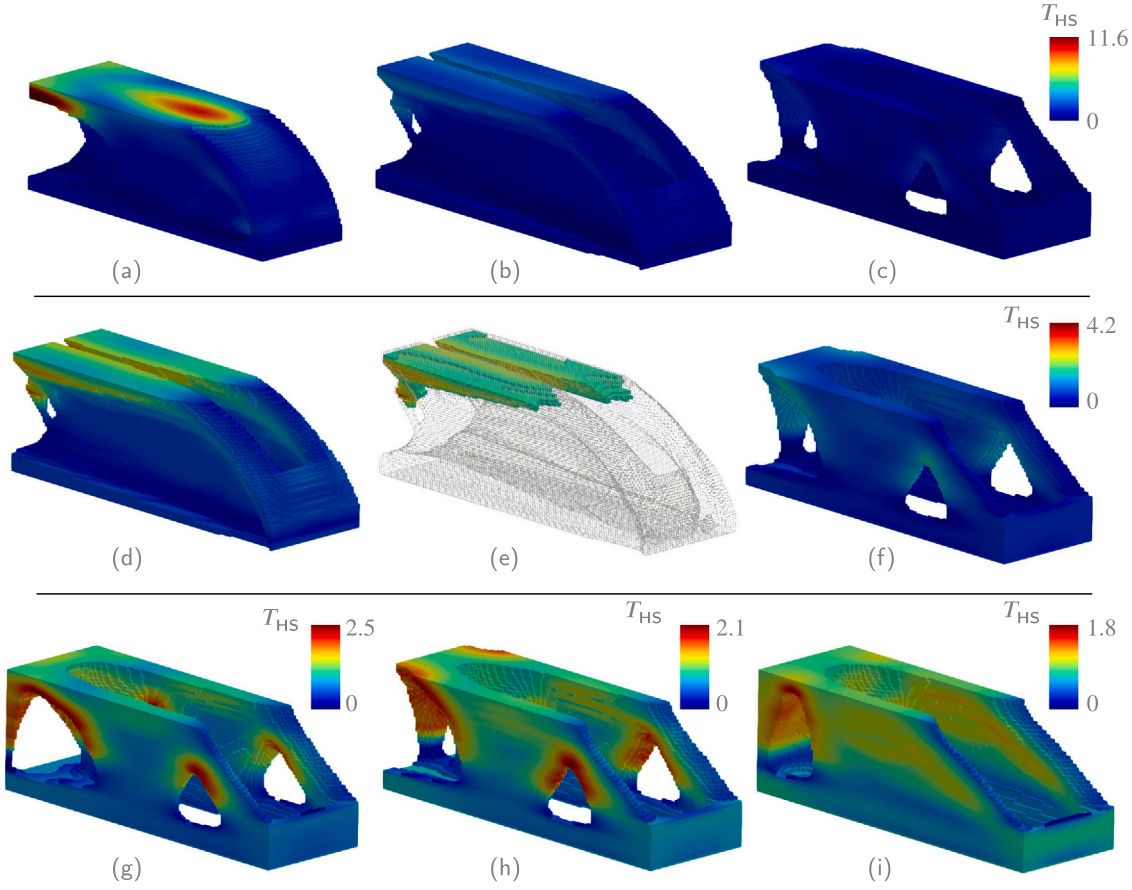

Fig. 7. Hotspot fields obtained for (a) standard TO design (b) AM-filter design (c) HS 45 design. For the sake of comparison, all three fields are shown with a common normalized temperature scale with values ranging between 0 and maximum value obtained for these designs. For a closer comparison between AM-filter and HS 45 designs, same hotspot fields are presented again in (d) and (f), respectively, with normalized temperature scale ranging between 0 and maximum value obtained between these two designs. The regions of AM-filter design which violate the hotspot constraint with $\hat{T} > \hat{T}^{cr}(\theta^{cr} = 45°)$ are highlighted in (e). Lastly, individual hotspot fields for HS 40, HS 45 and HS 50 designs are shown in (g), (h) and (i), respectively.

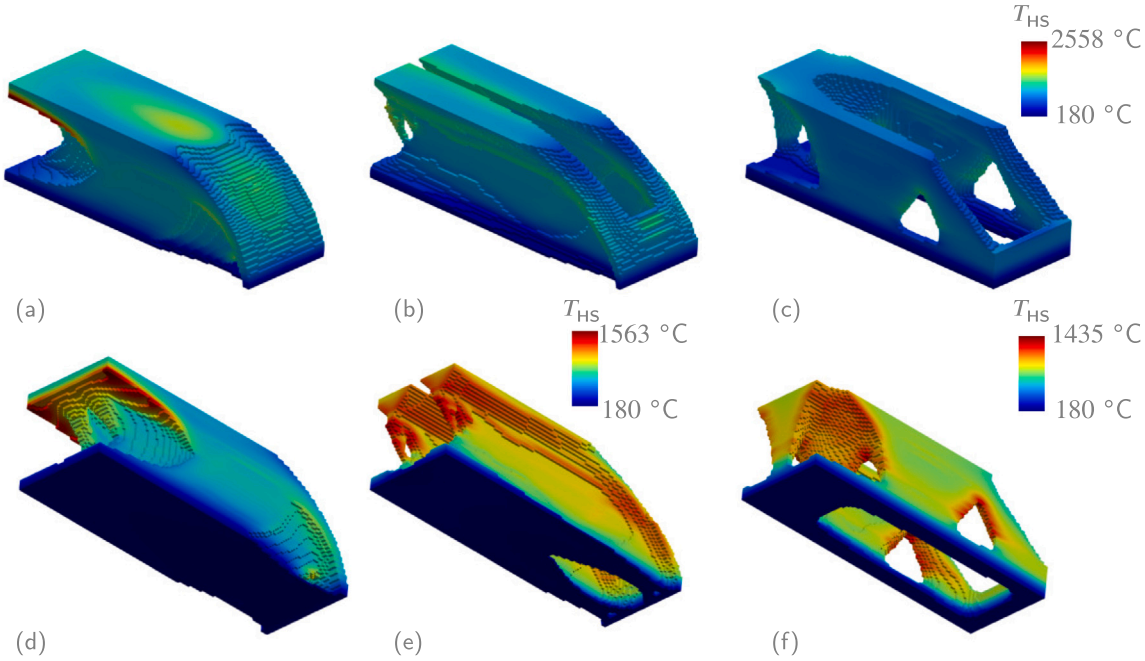

Fig. 8. The hotspot fields obtained using higher fidelity transient L-PBF simulation. (a) Standard TO (b) AM-filter and (c) HS 45 designs are shown with fields ranging between a common scale for comparison. The same designs are shown again from the back side with (e) AM-filter and (f) HS 45 designs hotspot fields ranging between baseplate temperature and maximum value obtained within respective designs.

found using simulation with different fidelity. The primary reason for this discrepancy is the gradual accumulation of heat that occurs as layers are deposited. A simplified steady-state model misses this aspect and hence only highlights the features which are responsible for local overheating. Nevertheless, in context of TO, the simplified model is able to capture crucial worst-case scenario information in an inexpensive manner, hence making it suitable for TO integration. Finally, using the higher fidelity simulation, it can be observed that HS 45 design shows lowest peak temperature of the three designs.

4. Experimental procedures

The L-PBF experiment was conducted using an EOS M290 machine equipped with a continuous fibre laser of maximum 400 W powder output. The feedstock powder used was Inconel 718 powder supplied by Höganäs Germany GmbH, with particle size ranging from 15 μm to 45 μm. The platform pre-heating temperature was set at 80 °C. The process chamber was flooded with argon gas and the oxygen level was kept under 1000 ppm throughout the build process. The parts were built with 310 W laser power, 800 mm/s laser scan speed, 0.11 mm hatch distance and 80 μm layer thickness. This set of parameters was previously optimized for nearly full density and high production speed. A stripe scan strategy was employed with a stripe width of 10 mm and 0.12 mm overlap between stripes. In each layer of the process, the laser scanning of the stripes is specified to traverse against the gas flow direction. The motivation behind this is to minimize the chances of process by-products being directed by the gas flow towards the laser scan pathway. This is achieved using the option available in EOSPRINT 2.8 software named as 'flow optimization'. Another machine feature named as 'downskin parameter settings' allows to automatically regulate laser power near overhanging features for better control of overheating. However, it was disabled for our experiments in order to clearly see and compare the overheating tendencies in different design features.

Three separate build jobs were run with build chamber configurations shown in Fig. 9. The first one is shown in Fig. 9(a) and referred to as Build 1. It comprised of five parts including the standard TO part, the three parts designed by the hotspot TO method, and the AM-filter TO part. As seen in Fig. 9(a), the parts were placed close to one another and occupy a large portion of the build area. It was found that the processing conditions deviated for the parts that extended to the edges and corners of the build plate. Similar observations have been reported in literature for other L-PBF systems [41–44]. For the EOS M290 machine used in the present study, the lower bottom corner (close to powder overflow and gas outlet) and the top right corner (close to the gas inlet and powder dispenser chamber) of the build area where the AM-filter part and the HS-TO 40 reside (see Fig. 9(a)) show re-occurrences of random hotspots throughout the build height. This could lead to local overheating issues not strictly related to the geometric layout of the part. Considering this, two more build jobs were run with two selected parts, namely the AM-filter part and the HS 45 part, placed at the centre of the build plate. These two are the most interesting samples in terms of overheating monitoring as they provide a direct comparison between a geometry-based method and a physics-based method. Note that, both relate to $\theta^{cr} = 45°$ with the former explicitly prohibiting overhangs lower than θ^{cr} while the latter uses the thermal conditions associated with 45° overhang as a threshold for overheating. The second and third build, referred to as Build 2 and 3, respectively, have different orientations between the part edges and the re-coating direction, see Fig. 9(b) and (c). This is motivated by the desire of examining the influence of re-coater direction on the OT data.

The experiments were monitored by an EOSTATE Exposure OT (optical tomography) system. The OT camera records near infrared radiations from the process area with an sCMOS camera having a band-pass filter at 900 nm ±12.5 nm. The sCMOS camera takes a long exposure image of the entire build area for each layer of the process with each pixel of the image corresponding to an area of 125 μm × 125 μm. Considering the build area is 250 mm × 250 mm, there are 2000 × 2000 pixels in each OT image. All images are stored in 16 bit format, hence the data ranges between 0 and 65 535. Due to this, this highest value of 65 535 is used as a normalization parameter so that all OT values are scaled between 0 and 1. The OT values from these images basically correspond to the integrated radiation over the period

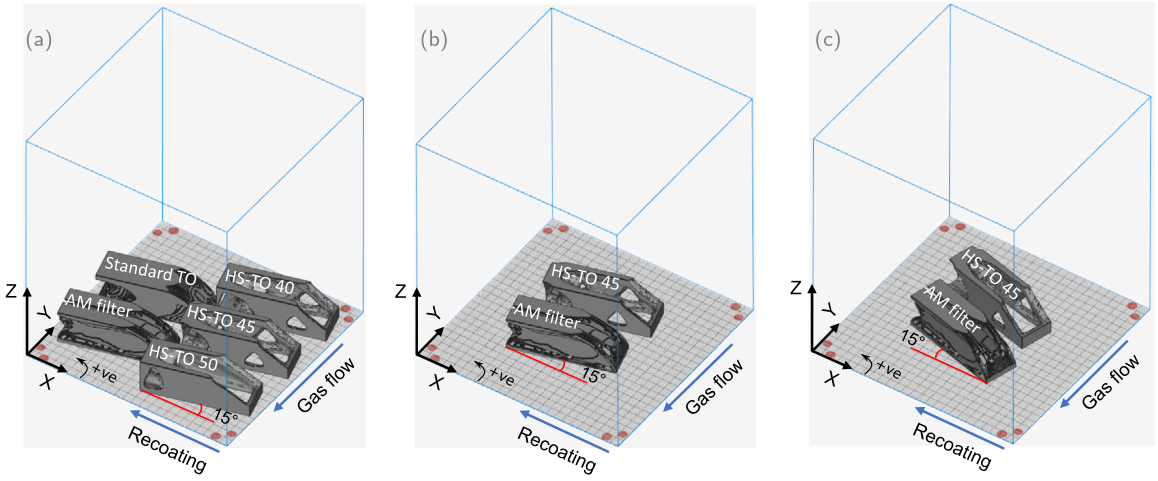

Fig. 9. Build layout for the three experiments with X, Y and Z representing the global co-ordinate axes for the build chamber. (a) Build 1 comprising five parts: Standard TO, AM-filter, HS 40, HS 45 and HS 50. (b) Build 2 with two parts: AM-filter and HS 45 such that long edges for the parts are oriented at +15° with respect to X axis. (c) Build 3 with two parts: AM-filter and HS 45 such that long edges for the parts are oriented at −15° with respect to X axis.

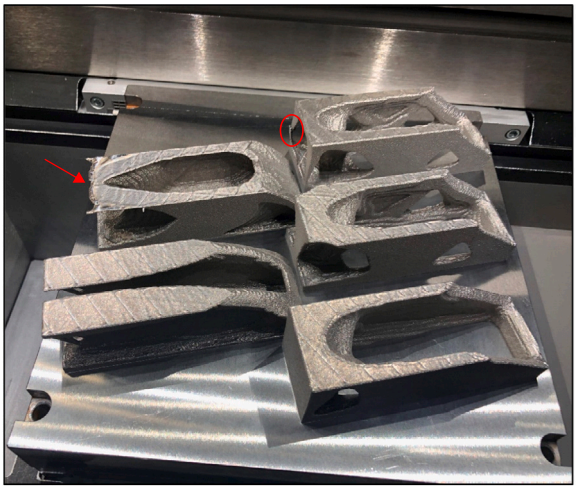

Fig. 10. Image of built parts in Build 1 configuration. The red arrow indicates the long overhang in standard TO part which caused recoater jamming. The thin wall in HS 40 design, marked with a red circle, fractured due to recoater collusion.

of time for each layer deposition. Hence, it is directly related to the total radiated energy over time and is thus an indication for overheating during the L-PBF process.

5. Results

Fig. 10 shows all the built parts in the Build 1 configuration where the long overhang of the standard TO part is marked with an arrow. There are a total 500 layers in each part, calculated as part height (= 40 mm) divided by layer thickness (= 0.08 mm). Each layer is recorded as one OT image which, when piled on top of each other, leads to a 3D data set with resolution of 2000 × 2000 × 500 voxels for the entire build chamber. Using the known location of samples, data corresponding to every sample is first extracted. Recall that each sample measured 120 mm × 40 mm × 40 mm and voxel size in x and y-axes is 125 μm while that in z-axis is 80 μm. It can be worked out that this leads to a resolution of 960 × 320 × 500 voxels in x, y and z directions, respectively, for each sample. This gives total 150 million voxels for each part. In order to conveniently visualize the 3D dataset, a convolution operation is performed over each layer where 3 and 2 voxels are averaged together in x and y-directions, respectively. This operation leads to a 3D dataset with 26 million voxels and makes it possible to easily visualize the obtained data. Note that this convolution operation is done only for the 3D visualization purpose while all other data analysis operations are performed on the non-convoluted data set.

The visualizations of 3D OT data is presented in Section 5.1. From the visualizations, it is found that the scanning strategy directly influences the OT values. This effect is discussed in detail in Section 5.2. Lastly, the data is used for comparing the overheating tendencies of different designs and a quantitative discussion is given in Section 5.3.

5.1. Data visualization and first impressions

Fig. 11 presents the 3D OT data fields obtained using the aforementioned convolution operation. The data is only shown for values ranging between 0.5 and 1 as lower values are less significant and obstruct the visualization of critical hotspots. As the standard TO makes no consideration for the manufacturability of the L-PBF design, it is as expected that some process issue would occur. In the experiment, the standard TO part experienced severe overheating, which led to significant thermal distortion and collision with the recoater. The build process was interrupted when a significant thermal distortion happened at the left edge of the TO part as the recoater was jammed at the raised edge, as indicated in Fig. 10. The building of the standard TO optimization was then cancelled manually at a build height of 34.7 mm (layer no 433) and the building of the remaining four parts continued. The 3D OT data field for standard TO design obtained from Build 1 is shown in Fig. 11(a) (front) and (d) (back). High OT values close to 1 can be seen near the long overhang. This is in accordance with the hotspot field presented in Fig. 7(a) where this long overhang caused high normalized temperatures. Lastly, the thin wall at the back of the HS 40 part fractured due to recoater collision, encircled in Fig. 10.

Further, as discussed in Section 4, the OT data for the AM-filter part obtained from Build 1 contained random noise due to improper gas flow. Also, it was found by comparing the data from Build 2 and 3 that part orientation with respect to re-coater has negligible effect on OT data. Hence, data from Build 2 and 3 were averaged for creating visualizations shown for AM-filter and HS 45 parts in Fig. 11(b),(e) and (c),(f), respectively. It can be seen in the AM-filter design that funnel shaped 45° overhangs indeed lead to high OT values, *i.e.* they remain at higher temperature for longer duration. This is in direct accordance with the hotspot fields shown in Fig. 7(e) where these funnels were identified as zones of heat accumulation using simplified L-PBF model. Lastly, as a first observation, the HS 45 degree design shows reduced

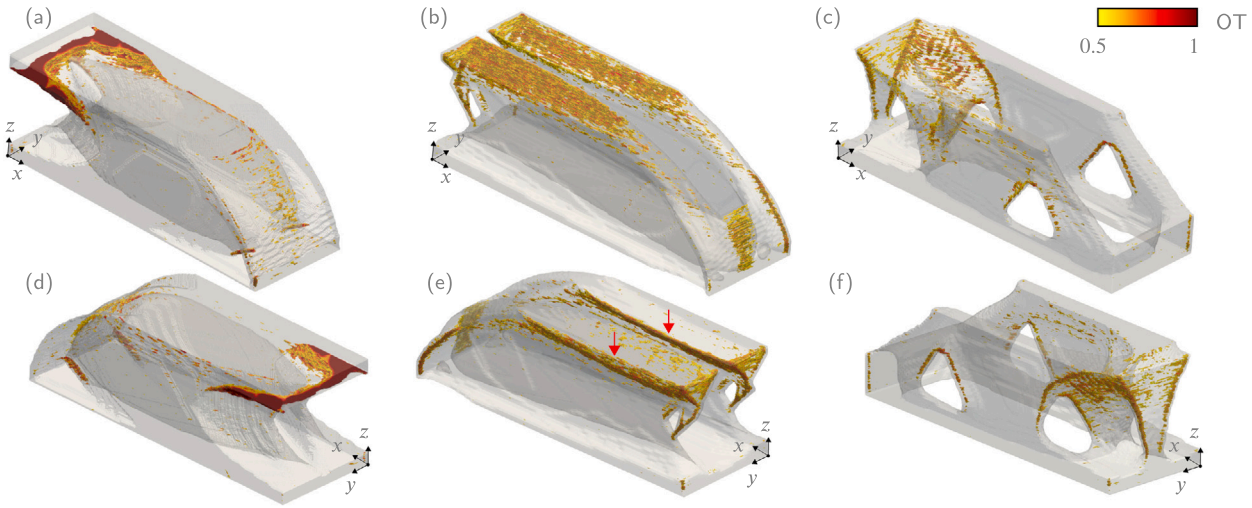

Fig. 11. Visualization of convoluted OT data for (a) and (d) Standard TO design obtained through Build 1 (b) and (e) AM-filter design obtained by averaging over Build 2 and 3 (c) and (f) HS 45 design obtained by averaging over Build 2 and 3. Here, only data above 0.5 is shown as it represents the possibility of overheating.

intensity of high OT values. A more quantitative comparison is given in Section 5.3.

A close observation of the 3D hotspot fields for AM-filter and HS 45 parts reveals that one side of overhanging features shows a higher tendency for overheating than the other side, even though, the parts are symmetrical. For example, note that in Fig. 11(e), one side of the funnels manifest high OT intensity (indicated by red arrow) while the other symmetric side shows a lower intensity. A similar observation can be made for HS 45 in Fig. 11(c) and (f). This directional distribution of overheating is found to be caused by scanning strategy and the effect is discussed in detail in the next section.

5.2. Influence of short hatches

As the local heat transfer conditions varies with part geometry, the OT values are found to be higher at overhangs which is in accordance with the simplified L-PBF thermal model. However, the overhangs are not the only source of hotspots in the OT images and it is found that high OT values or local overheating can also be caused by short scanning vectors. Fig. 12(a) shows a schematic presenting the scanning strategy used in this experiment. Here, the stripe scan strategy divides the exposure area into a number of stripes with a fixed width of 10 mm as specified by the operator. The scan vectors are placed perpendicular to the strip boundaries and the laser moves in a serpentine pattern shown in Fig. 12(a) starting from point S and terminating at point E. Inevitably there are shorter converging scan vectors at the corners and edges of the parts where a scan terminates, one such point marked by E in Fig. 12(a). In a short-hatched corner, the laser scans back and forth in a confined zone for a shorter period of time, allowing less time for heat extraction from the melted zone. The laser heat therefore accumulates locally and creates a hotspot. The starting spot for the laser, marked as point S, also remains in vicinity of short hatches. However, in this case, the scan vectors are increasingly larger, allowing more time for heat dissipation. This leads to asymmetrical heat accumulation towards the end of the laser path.

An OT image of layer number 456 for the AM-filter part is shown in Fig. 12(b). Here, this asymmetrical effect is clearly seen with high OT values only on one side of the overhangs. It is noteworthy here that high OT values in Fig. 12(b) are a combined effect of an overhang feature as well as short hatches. Another OT image for layer number 16 is shown in Fig. 12(d). Here also short hatches are present similar to layer number 456. However, they alone do not lead to high OT values, signifying the role of overhangs. Although, in case of thin features, hatches are inevitably short and they alone can cause high OT values. For example, the thin wall marked in Fig. 12(c) shows high OT values mainly due to short hatches. The stripe orientation is rotated by 67° between neighbouring layers. Therefore, the location of short hatches keeps changing for consecutive layers. It is inevitable to avoid short hatches and it is desirable that a design should not manifest overheating even with presence of short hatches.

5.3. Comparison for evaluating overheating behaviour

In this subsection, data analysis is done on the OT values found for the AM-filter and HS 45 designs. As discussed earlier, data from Build 2 and 3 is averaged for both the samples while data from Build 1 is not considered due to noise. In order to analyse the spatial distribution of OT data inside the samples, the normalized data is divided into packets of equal size and the volume it occupies in different designs is compared. This gives an idea about which design has a larger density of high OT values signifying that a larger portion of it remained at an elevated temperature for a longer duration during the build. Fig. 13(a) presents this comparison where the percentage range of the OT data is marked on the horizontal axis and the corresponding percentage volume it occupies is shown in form of a bar chart. Once again, data above 0.5 or 50% is used as it more critical and signifies possible overheating. Moreover, Fig. 13(b) shows a closeup view for the same bar chart for data above 70% as this is most critical for overheating. The error bars signify the range of variation in corresponding percentage volumes across Build 2 and 3. It is evident that for any given range of OT data, the HS 45 design occupies less volume than that of the AM-filter design. Also, it can be calculated by adding up percentage volumes that 20% of the AM-filter volume is above 50% of the OT data while only 12% volume is above 50% for HS 45 design.

Due to the gas flow issues with Build 1, the HS 40 design which was placed in the top right corner suffered from noisy OT data, making it difficult to draw any conclusions. The HS 50 design data from Build 1 was analysed and it showed a lower density of high OT values as compared to HS 45, with 9% volume occupying OT data with 50% value. This is as expected since increasing $\hat{T}^{cr}$ makes the design less prone to overheating.

5.4. Correlation with defects

In order to analyse the correlation between overheating and part quality, an investigation is carried out focused on identification of defects within the printed parts. It is reported in the literature that the excess energy deposited due to overheating can lead to keyhole

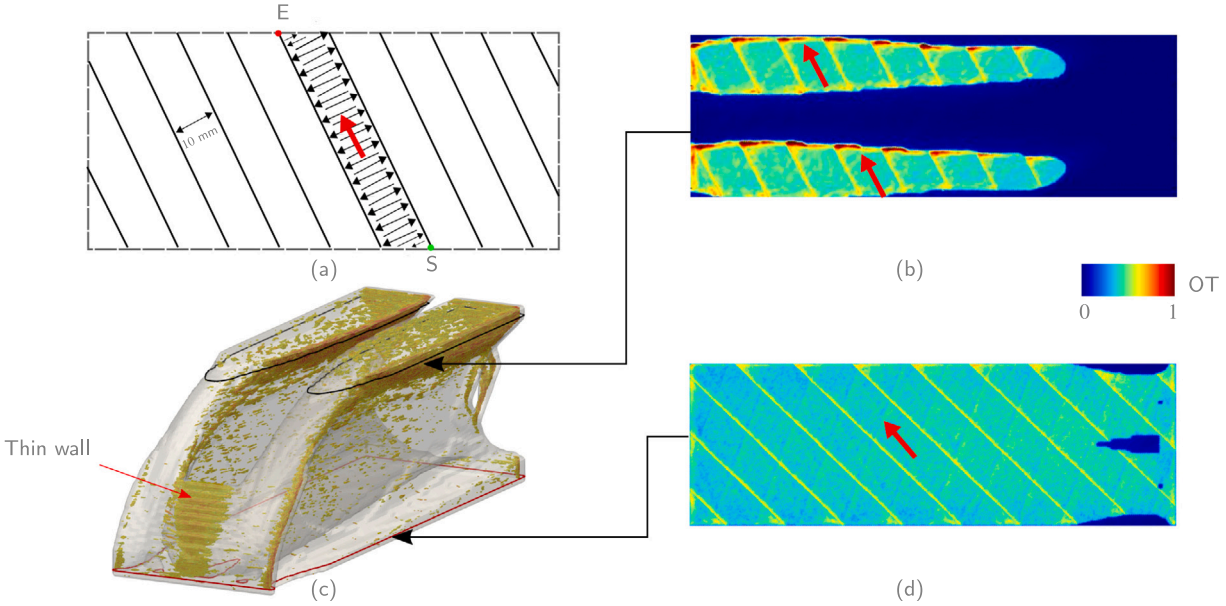

Fig. 12. Influence of short hatches on OT data. (a) A schematic representation of the scanning strategy used in this experiment where entire layer is first divided into number of stripes which are then scanned using a serpentine path. Short and converging hatches lead to local heat accumulation in vicinity of point E. (b) OT image for layer number 456 demonstrating high OT values near overhanging feature due to short hatch effect. (c) The 3D OT data field for AM-filter part showing the directional increase in high OT values due to short hatch effect. The front thin wall also shows high OT values due to short scanning vectors. (d) OT image for layer number 16 demonstrating that short hatches alone do not cause high OT values.

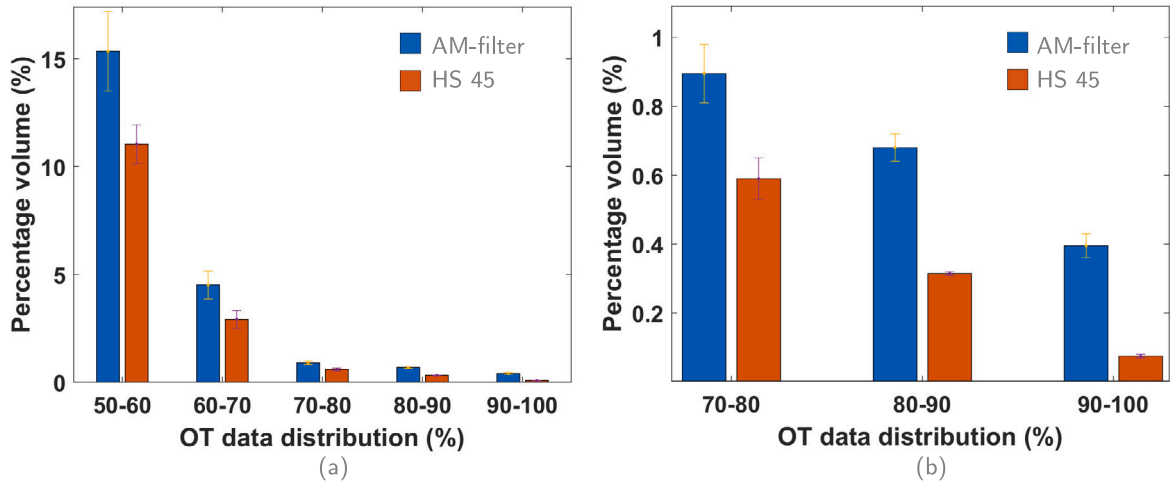

Fig. 13. Comparison of OT data distribution by part volume it occupies for the AM-filter and the HS 45 designs. The results are averaged over the data obtained from Build 2 and 3. The error bars indicate the variation in the values of percentage volumes over both the builds. (a) shows data above 50% while (b) highlights the distribution for data above 70% as it is more critical from the context of overheating.

porosity [45,46]. Hence a quantitative analysis of porosity is performed to identify the relationship between defects and overheating indicated by high OT values. For this purpose, the fabricated pieces were cut using Electron Discharge Machining (EDM) to obtain multiple cross-sections for analysis of defects. The samples were mounted in polymer resin, ground and polished to obtain mirror-finish following standard metallographic sample preparation steps. Optical images were taken using a ZEISS-AxioScope7 optical microscope across the entire cross sections of samples by taking consecutive images with 10% overlap between each. The images were then combined to form a single image file for analysis.

Fig. 14 shows the AM-filter part with cuts marked at x = 1.5 mm, 3.0 mm, 5.2 mm, 24.6 mm and x = 44.6 mm and these sections are subsequently labelled as A^{AM},B^{AM},C^{AM},D^{AM} and E^{AM}, respectively. The cross-section locations are decided based on the OT observations such that defects can be analysed across a wide range of OT values. As suggested by thermal simulations in Section 3.2.4 and observed by OT experiments in Section 5.1, the funnel like shapes in the AM filter designs are identified as thermal bottlenecks. Hence, they are selected for analysis in the obtained cross-sectional images. In Fig. 14, the OT data maps corresponding to the cross-sections are presented. In order to adequately quantify the OT values associated with a particular cross-section, first a thresholding operation is performed. Since focus here remains on keyhole defects which are typically associated with excess energy deposition, it was deemed suitable to use a high threshold value of 0.8. Recall that OT values ranges between 0–1 while the population density of high OT values on a cross-section signifies the level of overheating. Therefore, to quantify a cross-section's OT value, the area of the cross-section where the OT values are above the threshold value 0.8 is multiplied with the mean OT value of this area and indicated by $\overline{OT}$. The corresponding $\overline{OT}$ values are given in Fig. 14 for each

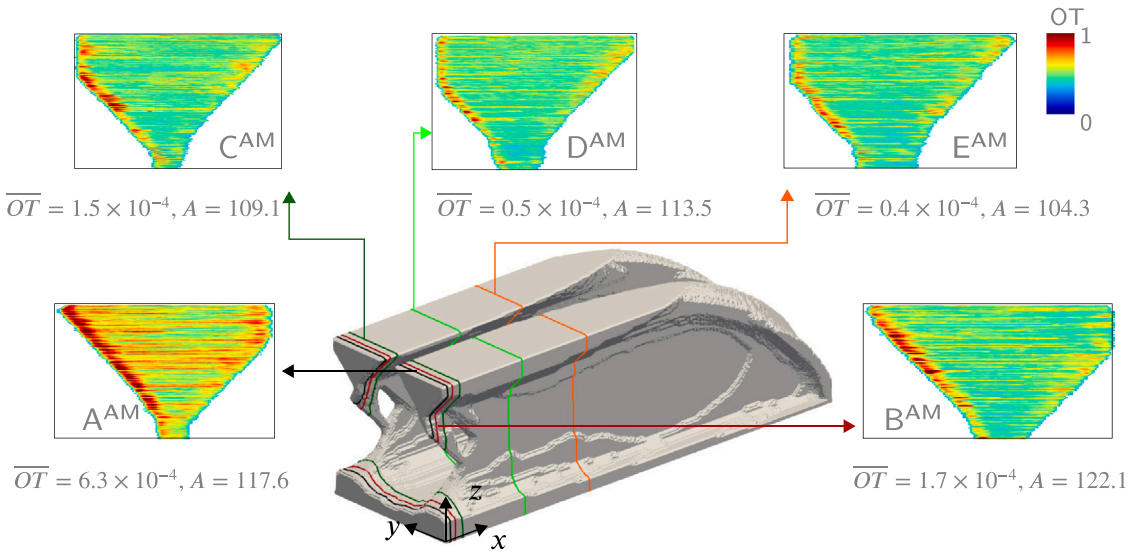

Fig. 14. The AM-filter part is cut at 5 sections locations at $x = 1.5$ mm, 3.0 mm, 5.2 mm, 24.6 mm and 44.6 mm on the $y - z$ plane. The OT maps for the funnel like shapes are shown and labelled in sequence of increasing x coordinates. The critical OT area $\overline{OT}$ and total area of the funnel shapes A are also provided in mm^2 for each cross-section.

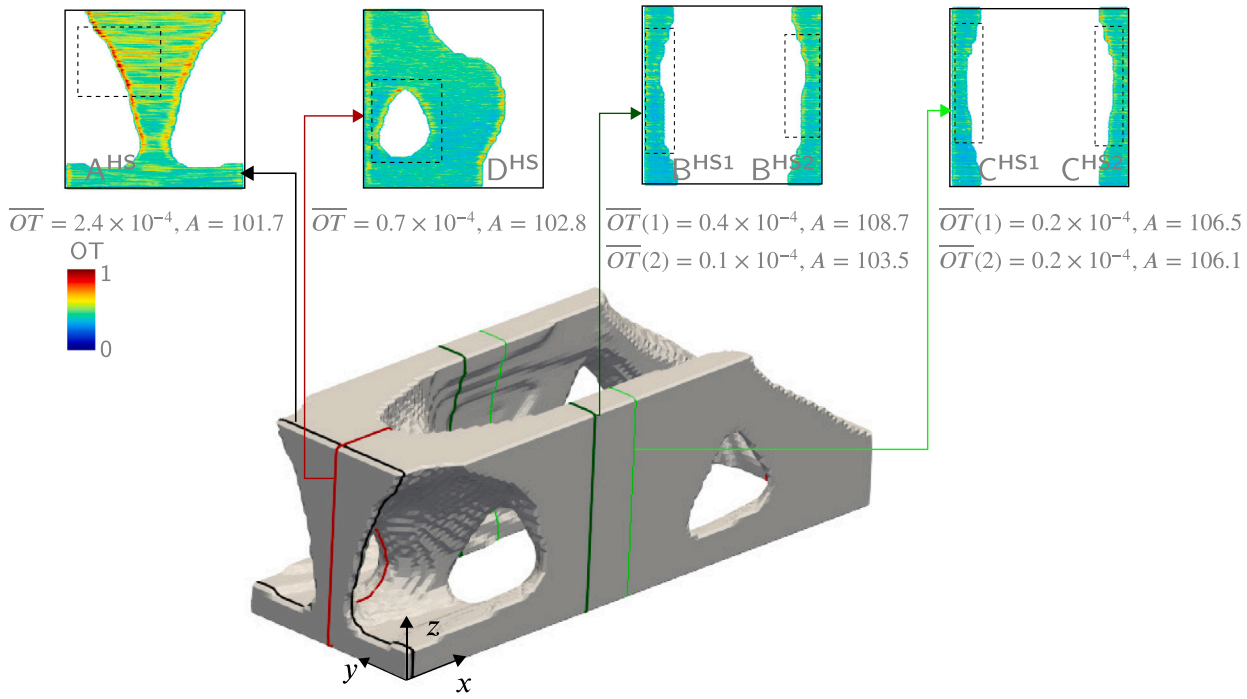

Fig. 15. The HS 45 part is cut at 4 locations at $x = 1.5$ mm, 46.5 mm, 57.0 mm and $y = 20.0$ mm. The OT maps for the sections are shown and these sections are labelled as A^{HS} to C^{HS} with increasing x coordinates while the section along $x - z$ plane is numbered as D^{HS}. Note that cross-section B and C provide two disjointed sub-sections each and they are treated as an individual section, referred to as '*1*' and '*2*' in the analysis. Here, cross-section A^{HS} shows relatively highest OT values while all other cross-sections have considerably low OT values. This is also exemplified by the $\overline{OT}$ values provided for each cross section. Lastly, the surface area Ω of the region enclosed within the dotted rectangles are also reported. Both $\overline{OT}$ and Ω are in mm^2.

cross-section and it can be seen that cross-section A^{AM} shows highest $\overline{OT}$ value. Similarly, the HS45 sample was cut at 4 locations located at $x = 1.5$ mm, 46.5 mm, 57 mm and $y = 20$ mm as shown in Fig. 15. These are labelled as A^{HS},B^{HS},C^{HS} and D^{HS} and note that cross-section C^{HS} and D^{HS} provide two disjointed sub-sections that are treated individually for the analysis, hence in total six cross-sections are analysed. The OT maps, critical OT area and $\overline{OT}$ values are also marked in Fig. 15. Lastly, the total areas Ω associated with the cross-sections are also reported and used for defect calculation explained below.

The images for A^{AM} and B^{AM} are shown in Fig. 16(a) and (b), respectively, while that for A^{HS} is presented in Fig. 16(d). Here, only images corresponding to the three highest critical OT area values $\overline{OT}$ are presented for the sake of brevity while all remaining images are provided as supplementary material. In order to quantify the amount of porosity, the cross-section images are subjected to a Matlab based boundary tracing algorithm and pore boundaries found are indicated in red colour in Fig. 16. The image resolution is such that each pixel measures 0.88 μm ×0.88 μm. In order to develop a quantitative measure of porosity associated with each cross-section image, first a shape analysis step is carried out which uses the concept of Feret diameter d_f for classifying pores as defects [47]. The Feret diameters associated with pore shapes are calculated using the boundary information and

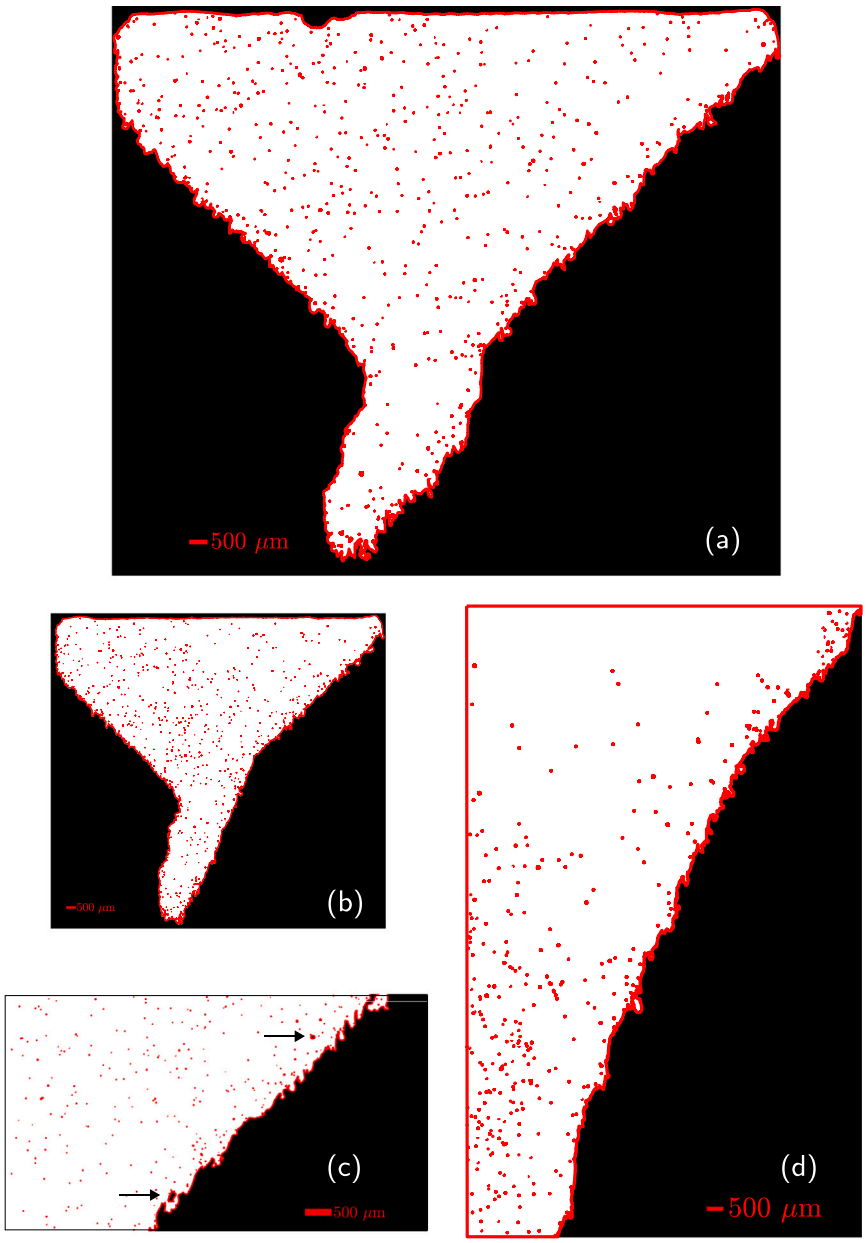

Fig. 16. Cross-sectional images obtained for (a) A^{AM} (b) B^{AM} (c) C^{AM} (magnified to highlight defects) and (d) A^{HS}. A Matlab based boundary tracing algorithm is used to identify pores indicated in red colour.

then pores with d_f larger than 10 μm are considered while others are discarded. Fig. 16(c) highlights two such pores from the image obtained from C^{AM} where large pores near the overhang surface can be observed. Such pores can induce stress concentration and adversely influence mechanical properties [45]. A parameter called pore area fraction is calculated for every cross-section. It is given by $\frac{\sum_{i=1}^{n} a_i}{\Omega}$ where a_i represents area of the ith pore associated with a particular cross-section while Ω represents total area of the cross-section. The areas for every cross-section are reported in Figs. 14 and 15. Given the stochastic nature of pore formation, it is deemed more appropriate to consider sections with similar area values across samples. Therefore, sub-sections are considered from the larger sections of HS 45 design so that the considered areas are similar to that of AM-filter design. These sub-sections are marked on the OT maps in Fig. 15 using dotted rectangles and areas of the regions enclosed within these rectangles are also reported. It is ensured that these sub-sections also encapsulate high OT regions.

Finally, Fig. 17 shows the variation of pore fraction area with respect to critical OT area for all 11 sections from both designs. The data points in red are from the AM-filter design and data points in green belong to the HS 45 design. It can be observed that propensity of pore formation increases with increasing regions of high OT values. For example, AM-filter cross-section A^{AM} in Fig. 14 has the largest $\overline{OT}$ value and is reported to have the highest pore area fraction as well. On the other extreme, it can be seen that sections with lower $\overline{OT}$ values tend to have a lower pore area fraction, signified by the data points located in the lower left corner of Fig. 17. However, the data points located in between these two extremes show a less consistent pattern. The results presented here show a broad trend which is consistent with the common understanding that higher energy density or high OT values will increase the likelihood of pore formation. Nevertheless, it is well-known that local melt-pool physics significantly influence the mechanism of keyhole formation and there could be factors other than geometry-induced local overheating which could influence pore

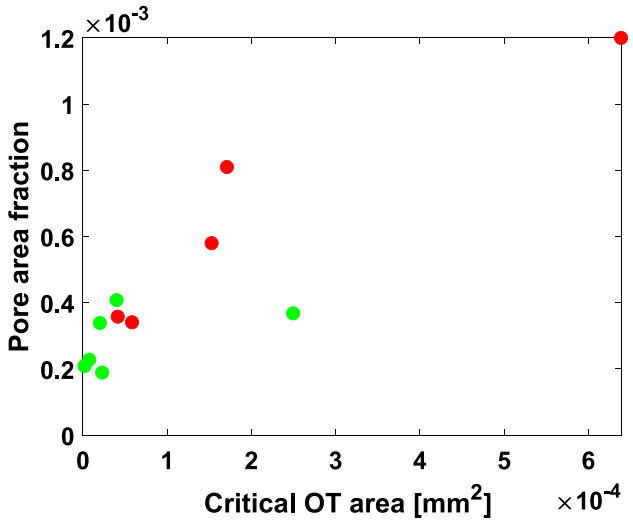

Fig. 17. The variation of pore area fraction with respect to respective critical OT area $\overline{OT}$. It is evident that $\overline{OT}$ values for HS 45 cross-sections remain on the lower side resulting in lower pore formation as compared to the AM-filter design.

formation, for example, anomalous behaviour of gas flow [45]. These effects require further investigation which is beyond the scope of this paper.

6. Discussion

The reported experimental investigation demonstrates that the proposed physics-based hotspot TO method can efficiently generate designs which are less prone to overheating and are less likely to manifest the defects associated with overheating, such as porosity. On the other hand, widely popular geometry-based TO schemes do not ensure overheating avoidance as the thermal behaviour is not uniquely linked with overhang angles. In order to emphasize this point, Fig. 18(a) and (b) show the AM-filter and HS 45 designs, respectively, with STL facets which have overhang angles less than $\theta^{cr} = 45°$ marked in red colour. It is evident that AM-filter design is largely free from such overhang violations and the combined area of such facets for AM-filter design is found to be 248 mm^2. Note that all such facets are near the baseplate and it is suspected that these are results of iso-surface extraction as the AM-filter strictly prohibits such facets. Contrary to this, the combined area of facets with overhang angles less than $\theta^{cr} = 45°$ for the HS 45 design is 438 mm^2 and these facets are located in multiple zones. In spite of this, as shown in Sections 5.3 and 5.4, the trend for overheating is opposite where the HS 45 design has a lower density of high OT values. This is due to the funnel shapes (marked with arrows in Fig. 18(a)) in the AM-filter design which, although satisfy the overhang criteria, act as a thermal bottleneck causing heat accumulation which leads to high OT values. This demonstrates that local thermal behaviour does not uniquely depend on overhang angle. Instead it is governed by the combined heat evacuation capacity of neighbouring features.

The hotspot TO focuses on geometry induced overheating and the influence of scanning pattern is not included within the simplified L-PBF model. However, it is found from the OT data that short and converging scans can aggravate overheating tendencies associated with geometric features. Note that the choice of a scanning pattern is mainly based on relieving the residual stresses in successive layers and often predetermined. It is noteworthy that both the AM-filter and HS 45 designs encountered short hatches during fabrication as both were subjected to similar scanning patterns where laser movement was directed against the gas flow. The AM-filter design has several funnel shaped features close to 45° which, in combination with short hatches, lead to high OT values. The HS 45 design, even with similar short hatches, leads to lower OT values since it is designed for efficient heat evacuation. Nevertheless, the findings here suggest that it will be beneficial to consider the influence of scanning strategy during designing the part. Alternatively, a scan pattern optimization can potentially be done based on a given part design.

The main aim of this paper was to thoroughly examine the phenomenon of overheating in L-PBF and investigate its root causes. Overheating directly affects part quality, yet there are also several after effects associated with the thermal history, for example, development of high residual stresses and associated part-distortions, which are potentially critical and need attention for achieving defect-free parts. In this context, several researchers have thoroughly investigated the relationship between thermal history and residual stresses and it is established that, typically, local overheating or heat accumulation increases the magnitude of generated residual stresses. More precisely, Parry et al. [48] presented numerical results demonstrating that zones prone to local overheating lead to high residual stresses while Ali et al. [49] investigated this relationship experimentally and found that high cooling rates are directly responsible for increasing residual stresses. Based on these studies, it is anticipated that the designs generated by the novel Physics-based TO method presented in paper will perform better in the context of residual stress formation as well. Nonetheless, it is also observed that residual stress development during L-PBF does not exclusively depend on the part's thermal history and mechanical boundary conditions imposed by layer geometries also influence it. In this regard, a TO method which includes a dedicated L-PBF model which accounts for the complete thermo-mechanical response during the process is more likely to fully guarantee defect-free designs. However, such a model still remains computationally intractable and hence, its integration with TO remains a challenging endeavour.

Here, a quantitative investigation was done co-relating overheating with defects. For this purpose, a total of 9 cuts were made which revealed useful insights. However, an even deeper analysis can be carried out by performing volumetric analysis and analysing more regions of the parts. For example, computer tomography (CT) can be used to capture defects and associate them with high OT values. Another possible option is to perform a microstructural evaluation of the critical zones. These studies can potentially identify the limiting OT value which can be treated as threshold for a quantitative definition of overheating.

While the numerical examples and experimental investigations shown in this paper demonstrate that the novel physics-based hotspot TO can be applied successfully, its limitations should also be reported. First, the simplified L-PBF model which is integrated with TO here captures the overheating tendencies associated with design features in a qualitative manner. However, it is an approximation of the thermal interactions which occur during the process and only focuses on capturing overheating. A higher fidelity model, *e.g.* including transient heat transfer and/or mechanical analysis, will be able to address other important process characteristics, such as cooling rates, residual stresses and deformations. A model which could include the influence of hatch scanning will also be beneficial in developing a design which remains robust against process uncertainties. In this context, the challenge of high computational cost associated with the higher fidelity L-PBF models needs to be addressed. Another limitation is that a single build orientation is considered, which cannot change during the optimization. While there are multiple factors which dictate the choice of build direction (part height, surface finish, support accessibility, etc.), it would be beneficial to develop a generalized formulation where build orientation is simultaneously optimized.

7. Conclusions

This paper presents a TO method which utilizes a simplified thermal model of the L-PBF process for generating designs less prone to

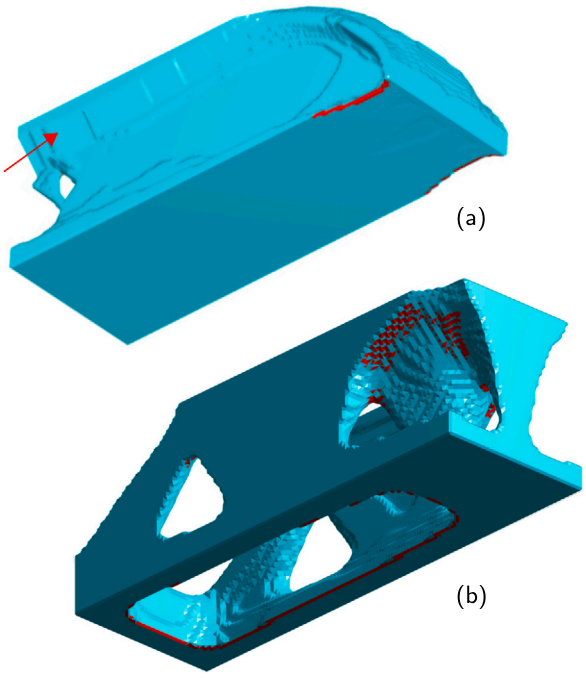

Fig. 18. STL facets which have overhang angles less than $\theta^{cr} = 45°$ are marked red for (a) AM-filter and (b) HS 45 designs.

overheating defects. The simplified model makes it possible to integrate L-PBF process physics within the optimization while remaining computationally tractable. The capability of the novel TO method is compared experimentally with two other TO approaches, standard TO and geometry-based overhang control (AM-filter) TO. Designs obtained using all three TO methods are fabricated using L-PBF and the process is monitored using optical tomography (OT). It was found by comparing OT data, which is an indicator of overheating, that standard TO which does not address manufacturability, leads to severe overheating and build failure. Further, comparing TO methods which include AM constraints, the design obtained by the novel TO method presented in this paper shows a significant reduction in overheating compared to the AM-filter design. Finally, a correlation between overheating and defects was shown. These observations reveal that overheating is not uniquely linked to an overhang angle, and commonly used guidelines of avoiding acute overhangs are insufficient for avoiding overheating.

The hotspot TO uses a simplified L-PBF model and realizes 3D designs which show reduced risk of overheating. The proposed method with experimental validation presents a promising opportunity for addressing AM physics within the optimization loop with carefully selected simplifications [17]. Nevertheless, there are certain improvements that can be considered. As discussed in Section 3, a constant slab thickness of $s = 12$ mm is used in this paper which is calculated based on the concept of thermal characteristic length. A more detailed numerical study can be done to for estimating the slab thickness value. For example, Moran et al. [33] presented a framework for determining thermal interaction length using higher fidelity AM simulations. Next, the influence of machine parameters, such as downskin settings, baseplate pre-heat temperature, laser power and velocity etc. was not investigated here for simplicity but can be considered in future. Further, it was found that short and converging hatches also significantly influence the overheating behaviour. Since the hotspot TO method is based on a layer-by-layer simulation, such detailed effects related to specific scan patterns are not captured and inclusion of more detailed models is necessary to address this. In this regard, developing similar computationally inexpensive models which can accurately capture more complicated physics-based parameters, *e.g.* scanning effects, residual stresses, deformation, is seen as an important avenue for future research.

CRediT authorship contribution statement

R. Ranjan: Writing – original draft, Validation, Methodology, Investigation, Formal analysis, Data curation, Conceptualization. **Z. Chen:** Writing – original draft, Visualization, Validation, Methodology, Investigation, Formal analysis, Data curation, Conceptualization. **C. Ayas:** Writing – review & editing, Supervision, Project administration, Investigation, Funding acquisition, Formal analysis, Conceptualization. **M. Langelaar:** Writing – review & editing, Supervision, Resources, Project administration, Methodology, Investigation, Funding acquisition, Conceptualization. **F. Van Keulen:** Writing – review & editing, Supervision, Resources, Project administration, Investigation, Funding acquisition, Conceptualization.

Declaration of competing interest

The authors declare that they have no known competing financial interests or personal relationships that could have appeared to influence the work reported in this paper.

Data availability

Data will be made available on request.

Acknowledgements

This work was performed within PAM^2, 'Precision Additive Metal Manufacturing', a research project funded by The EU Framework Programme for Research and Innovation - Horizon 2020 - Grant Agreement No 721383. The experiments were funded by the Centre for Additive Manufacture–Metal (CAM^2) supported by the Swedish Governmental Agency for Innovation Systems (Vinnova).

Appendix A. Sensitivity analysis of the hotspot constraint

The sensitivity of the thermal constraint given by Eq. (2) with respect to design variable ρ is derived using the adjoint method. As described in Section 2, design is divided into a set of overlapping slabs and a steady-state heat equation is solved for each slab. For this purpose, first the global conductivity matrix $\mathbf{G}$ and thermal load vector $\mathbf{Q}$ are assembled. Next, a set of discretized steady-state heat equations given by

$$\mathbf{G}^{(J)}\hat{\mathbf{T}}^{(J)} = \mathbf{Q}^{(J)} \quad \forall \quad J \in [1, m] \tag{3}$$

is solved numerically using FEA and nodal temperatures $\hat{\mathbf{T}}^{(J)}$ are obtained for Slab J. Here, J varies from 1 to m with m representing total number of slabs. Recall that we are only interested in maximum temperatures which occur at the topmost nodes. Next, the relation between the temperature for the Jth slab $\hat{\mathbf{T}}^{(J)}$ and hotspot field $\hat{\mathbf{T}}$ is defined as

$$\hat{\mathbf{T}} = \sum_{J=1}^{m} \mathbf{L}^{(J)}\hat{\mathbf{T}}^{(J)}, \tag{4}$$

where $\mathbf{L}^{(J)}$ is a matrix prepared for extracting top node temperatures for the Jth slab and sequentially place them in $\hat{\mathbf{T}}$. Next, the constraint given by Eq. (2) is written in augmented form as

$$g^* = g + \sum_{J=1}^{m} (\lambda^{(J)})^T(\mathbf{Q}^{(J)} - \mathbf{G}^{(J)}\hat{\mathbf{T}}^{(J)}), \tag{5}$$

with $\lambda^{(J)}$ as the Lagrange multiplier vector for the J^{th} slab. Recall that filtering schemes are employed and hence element density $\tilde{\rho}_e$ is

different from design variable ρ. First, differentiating the augmented constraint with respect to element density $\tilde{\tilde{\rho}}_e$ gives

$$\frac{\partial g^*}{\partial \tilde{\tilde{\rho}}_e} = \frac{\partial g}{\partial \tilde{\tilde{\rho}}_e} + \sum_{J=1}^{m} (\lambda^{(J)})^T \left(\frac{\partial \mathbf{Q}^{(J)}}{\partial \tilde{\tilde{\rho}}_e} - \mathbf{G}^{(J)} \frac{\partial \hat{\mathbf{T}}^{(J)}}{\partial \tilde{\tilde{\rho}}_e} - \frac{\partial \mathbf{G}^{(J)}}{\partial \tilde{\tilde{\rho}}_e} \hat{\mathbf{T}}^{(J)} \right). \tag{6}$$

Expansion of the first term in the RHS of Eq. (6) gives

$$\frac{\partial g}{\partial \tilde{\tilde{\rho}}_e} = \frac{\left[\frac{1}{n} \sum_{i=1}^{n} (\hat{T}_i)^P \right]^{(\frac{1}{P})-1}}{nT^{\mathrm{cr}}} \left[(\hat{\mathbf{T}})^{P-1} \right]^T \sum_{J=1}^{m} \mathbf{L}^{(J)} \frac{\partial \hat{\mathbf{T}}^{(J)}}{\partial \tilde{\tilde{\rho}}_e}. \tag{7}$$

In order to avoid computation of state sensitivities, all the terms with $\partial \hat{\mathbf{T}}^{(J)} / \partial \tilde{\tilde{\rho}}_e$ are combined. This leads to the following sensitivity expression:

$$\frac{\partial g^*}{\partial \tilde{\tilde{\rho}}_e} = \sum_{J=1}^{m} \left(\lambda^{(J)} \right)^T \left(\frac{\partial \mathbf{Q}^{(J)}}{\partial \tilde{\tilde{\rho}}_e} - \frac{\partial \mathbf{G}^{(J)}}{\partial \tilde{\tilde{\rho}}_e} \hat{\mathbf{T}}^{(J)} \right). \tag{8}$$

Here, $\lambda^{(J)}$ is the solution of following equation:

$$\frac{\left[\frac{1}{n} \sum_{i=1}^{n} (\hat{T}_i)^P \right]^{(\frac{1}{P}-1)}}{nT^{\mathrm{cr}}} \left[(\hat{\mathbf{T}})^{P-1} \right]^T \mathbf{L}^{(J)} - (\lambda^{(J)})^T \mathbf{G}^{(J)} = 0, \tag{9}$$

where $J = 1, \ldots, m$. Furthermore, sensitivities with respect to the design variables are calculated using the chain rule:

$$\frac{\partial f^*}{\partial \rho} = \frac{\partial f^*}{\partial \tilde{\tilde{\rho}}_e} \frac{\partial \tilde{\tilde{\rho}}_e}{\partial \rho}. \tag{10}$$

Appendix B. Supplementary data

Supplementary material related to this article can be found online at https://doi.org/10.1016/j.addma.2022.103339.

References

[1] R. Leach, S. Carmignato, Precision Metal Additive Manufacturing, CRC Press, 2020.
[2] M.P. Bendsøe, O. Sigmund, Topology Optimization: Theory, Methods and Applications, Springer-Verlag Berlin Heidelberg, 2003.
[3] J. Liu, A.T. Gaynor, S. Chen, Z. Kang, K. Suresh, A. Takezawa, L. Li, J. Kato, J. Tang, C.C.L. Wang, L. Cheng, X. Liang, A.C. To, Current and future trends in topology optimization for additive manufacturing, Struct. Multidiscip. Optim. 57 (6) (2018) 2457–2483.
[4] R. Mertens, S. Clijsters, K. Kempen, J.-P. Kruth, Optimization of scan strategies in selective laser melting of aluminum parts With Downfacing Areas, J. Manuf. Sci. Eng. 136 (6) (2014).
[5] M. Cloots, L. Zumofen, A. Spierings, A. Kirchheim, K. Wegener, Approaches to minimize overhang angles of SLM parts, Rapid Prototyp. J. 23 (2017) 362–369.
[6] D. Wang, Y. Yang, Z. Yi, X. Su, Research on the fabricating quality optimization of the overhanging surface in SLM process, Int. J. Adv. Manuf. Technol. 65 (9) (2013) 1471–1484.
[7] A.P. Charles, A. Elkaseer, L. Thijs, V. Hagenmeyer, S. Scholz, Effect of process parameters on the generated surface roughness of down-facing surfaces in selective laser melting, Appl. Sci. 9 (2019).
[8] G. Mohr, S.J. Altenburg, K. Hilgenberg, Effects of inter layer time and build height on resulting properties of 316l stainless steel processed by laser powder bed fusion, Addit. Manuf. 32 (2020) 101080.
[9] D. Kastsian, D. Reznik, Reduction of local overheating in selective laser melting, in: In Proceedings of Simulation of Additive Manufacturing (SIM-AM), Munich, Germany, 2017.
[10] A.T. Gaynor, J.K. Guest, Topology optimization considering overhang constraints: Eliminating sacrificial support material in additive manufacturing through design, Struct. Multidiscip. Optim. 54 (5) (2016) 1157–1172.
[11] C. Wang, X. Qian, Simultaneous optimization of build orientation and topology for additive manufacturing, Addit. Manuf. 34 (2020) 101246.
[12] M. Langelaar, Topology optimization of 3D self-supporting structures for additive manufacturing, Addit. Manuf. 12 (2016) 60–70.
[13] M. Langelaar, An additive manufacturing filter for topology optimization of print-ready designs, Struct. Multidiscip. Optim. 55 (3) (2017) 871–883.
[14] E. van de Ven, R. Maas, C. Ayas, M. Langelaar, F. van Keulen, Overhang control based on front propagation in 3D topology optimization for additive manufacturing, Comput. Methods Appl. Mech. Engrg. 369 (2020) 113169.
[15] G.A. Adam, D. Zimmer, Design for additive manufacturing—Element transitions and aggregated structures, CIRP J. Manuf. Sci. Technol. 7 (1) (2014) 20–28.
[16] S. Patel, J. Mekavibul, J. Park, A. Kolla, R. French, Z. Kersey, G. Lewin, Using machine learning to analyze image data from advanced manufacturing processes, in: 2019 Systems and Information Engineering Design Symposium (SIEDS), Charlottesville, VA, USA, 2019, pp. 1–5.
[17] R. Ranjan, C. Ayas, M. Langelaar, F. van Keulen, Fast detection of heat accumulation in powder bed fusion using computationally efficient thermal models, Materials 13 (20) (2020).
[18] E. Denlinger, J. Irwin, P. Michaleris, Thermomechanical modeling of additive manufacturing large parts, J. Manuf. Sci. Eng. 136 (2014) 061007.
[19] N. Keller, V. Ploshikhin, New method for fast predictions of residual stress and distortion of AM parts, in: Solid Freeform Fabrication Symposium, Austin, Texas, 2014, pp. 1229–1237.
[20] O. Amir, Y. Mass, Topology optimization for staged construction, Struct. Multidiscip. Optim. 57 (4) (2018) 1679–1694.
[21] G. Allaire, C. Dapogny, A. Faure, G. Michailidis, Shape optimization of a layer by layer mechanical constraint for additive manufacturing, CR Math. 355 (6) (2017) 699–717.
[22] M. Zhou, Y. Liu, Z. Lin, Topology optimization of thermal conductive support structures for laser additive manufacturing, Comput Method Appl M 353 (2019) 24–43.
[23] M. Boissier, G. Allaire, C. Tournier, Additive manufacturing scanning paths optimization using shape optimization tools, Struct. Multidiscip. Optim. 61 (6) (2020) 2437–2466.
[24] R. Ranjan, C. Ayas, M. Langelaar, F.v. Keulen, Controlling local overheating in topology optimization for additive manufacturing, Struct. Multidiscip. Optim. 65 (6) (2022) 162.
[25] G. Zenzinger, J. Bamberg, A. Ladewig, T. Hess, B. Henkel, W. Satzger, Process monitoring of additive manufacturing by using optical tomography, AIP Conf. Proc. 1650 (1) (2015) 164–170.
[26] G. Mohr, S.J. Altenburg, A. Ulbricht, P. Heinrich, D. Baum, C. Maierhofer, K. Hilgenberg, In-situ defect detection in laser powder bed fusion by using thermography and optical tomography—Comparison to computed tomography, Metals 10 (1) (2020).
[27] P. Yadav, V.K. Singh, T. Joffre, O. Rigo, C. Arvieu, E. Le Guen, E. Lacoste, Inline drift detection using monitoring systems and machine learning in selective laser melting, Adv. Eng. Mater. 22 (12) (2020) 2000660.
[28] F. Van Keulen, R. Haftka, N. Kim, Review of options for structural design sensitivity analysis. Part 1: Linear systems, Comput. Methods Appl. Mech. Engrg. 194 (30–33) (2005) 3213–3243.
[29] W. Zhang, M. Tong, N.M. Harrison, Resolution, energy and time dependency on layer scaling in finite element modelling of laser beam powder bed fusion additive manufacturing, Addit. Manuf. 28 (2019) 610–620.
[30] M. Rombouts, L. Froyen, A. Gusarov, E.H. Bentefour, C. Glorieux, Photopyroelectric measurement of thermal conductivity of metallic powders, J. Appl. Phys. 97 (2004) 24905.
[31] J. Romano, L. Ladani, M. Sadowski, Thermal modeling of laser based additive manufacturing processes within common materials, Procedia Manuf. 1 (2015) 238–250, 43rd North American Manufacturing Research Conference, NAMRC 43, 8-12 June 2015, UNC Charlotte, North Carolina, United States.
[32] F.P. Incropera, D.P. DeWitt, Fundamentals of Heat and Mass Transfer, fourth ed., John Wiley & Sons, Inc., New York City, New York, 1996.
[33] T. Moran, D. Warner, N. Phan, Scan-by-scan part-scale thermal modelling for defect prediction in metal additive manufacturing, Addit. Manuf. 37 (2021) 101667.
[34] A.S. Agazhanov, D.A. Samoshkin, Y.M. Kozlovskii, Thermophysical properties of Inconel 718 alloy, J. Phys. Conf. Ser. 1382 (1) (2019) 012175.
[35] Y. Yang, M. Knol, F. van Keulen, C. Ayas, A semi-analytical thermal modelling approach for selective laser melting, Addit. Manuf. 21 (2018) 284–297.
[36] T.E. Bruns, D.A. Tortorelli, Topology optimization of non-linear elastic structures and compliant mechanisms, Comput. Method Appl. Mech. 190 (26) (2001) 3443–3459.
[37] K. Liu, A. Tovar, An efficient 3D topology optimization code written in Matlab, Struct. Multidiscip. Optim. 50 (6) (2014) 1175–1196.
[38] K. Svanberg, The method of moving asymptotes—a new method for structural optimization, Int. J. Numer. Methods Eng. 24 (2) (1987) 359–373.
[39] F. Wang, B. Lazarov, O. Sigmund, On projection methods, convergence and robust formulations in topology optimization, Struct. Multidiscip. Optim. 43 (2011) 767–784.
[40] O. Sigmund, Morphology-based black and white filters for topology optimization, Struct. Multidiscip. Optim. 33 (4–5) (2007) 401–424.
[41] Y.R. Chen, G. Vastola, Y. Zhang, Optimization of inert gas flow inside laser powder bed fusion chamber with computational fluid dynamics, 2018.
[42] B. Ferrar, L. Mullen, E. Jones, R. Stamp, C. Sutcliffe, Gas flow effects on selective laser melting (SLM) manufacturing performance, J. Mater Process. Technol. 212 (2) (2012) 355–364.
[43] M. Schniedenharn, F. Wiedemann, J.H. Schleifenbaum, Visualization of the shielding gas flow in SLM machines by space-resolved thermal anemometry, Rapid Prototyp. J. 24 (8) (2018) 1296–1304.
[44] X. Zhang, B. Cheng, C. Tuffile, Simulation study of the spatter removal process and optimization design of gas flow system in laser powder bed fusion, Addit. Manuf. 32 (2020) 101049.

[45] A.A. Martin, N.P. Calta, S.A. Khairallah, J. Wang, P.J. Depond, A.Y. Fong, V. Thampy, G.M. Guss, A.M. Kiss, K.H. Stone, C.J. Tassone, J. Nelson Weker, M.F. Toney, T. van Buuren, M.J. Matthews, Dynamics of pore formation during laser powder bed fusion additive manufacturing, Nature Commun. 10 (1) (2019) 1987.

[46] B. Cheng, L. Loeber, H. Willeck, U. Hartel, C. Tuffile, Computational investigation of melt pool process dynamics and pore formation in laser powder bed fusion, J. Mater. Eng. Perform. 28 (11) (2019) 6565–6578.

[47] W.H. Walton, Feret's statistical diameter as a measure of particle size, Nature 162 (4113) (1948) 329–330.

[48] L. Parry, I. Ashcroft, R. Wildman, Understanding the effect of laser scan strategy on residual stress in selective laser melting through thermo-mechanical simulation, Addit. Manuf. 12 (2016) 1–15.

[49] H. Ali, H. Ghadbeigi, K. Mumtaz, Residual stress development in selective laser-melted Ti6Al4V: a parametric thermal modelling approach, Int. J. Adv. Manuf. Technol. 97 (5) (2018) 2621–2633.